
PERGAMON

Journal of Quantitative Spectroscopy & Radiative Transfer 75 (2002) 177–220

Journal of Quantitative Spectroscopy & Radiative Transfer

www.elsevier.com/locate/jqsrt

Fast and accurate 4 and 6 stream linearized discrete ordinate radiative transfer models for ozone profile retrieval

Roeland F. van Oss[a], Robert J.D. Spurr[b,*]

[a] *Royal Netherlands Meteorological Institute, P.O.Box 201, 3730 AE De Bilt, The Netherlands*
[b] *Harvard-Smithsonian Center for Astrophysics, 60 Garden Street, Cambridge, MA 02138, USA*

Received 5 February 2001; accepted 14 March 2001

Abstract

The global and long-term measurement of ozone vertical and horizontal distributions is one of the most important tasks in the monitoring of the earth's atmosphere. A number of satellite instruments are capable of delivering ozone profile distributions from UV nadir backscatter measurements. Retrieval algorithms should be efficient enough to deliver profiles in real-time without compromising accuracy. Such algorithms require a radiative transfer model that can generate quickly and accurately both simulated radiances and Jacobian matrices of weighting functions. We develop fast and analytic 4 stream and 6 stream linearized discrete ordinate models designed to satisfy performance and accuracy requirements for such an algorithm. The models have the pseudo-spherical treatment of the direct beam attenuation. For anisotropic scattering we use the delta-M scaling method to deal with strong forward scattering peaks. We demonstrate that the accuracy of the models is improved greatly upon application of a single scatter correction based on an exact specification of the phase function. For wide-angle off-nadir viewing, a sphericity correction is developed to deal more precisely with attenuation in a curved atmosphere. Radiances and weighting functions for the 4 and 6 stream models are compared with 20 stream output from the LIDORT model. We show that for the UV range pertinent to ozone profile retrieval from space, the 4 stream model generates backscatter radiances to an accuracy $> 1.25\%$ for all viewing situations in a clear sky Rayleigh and background aerosol reference atmosphere, and up to 1.75% for a number of special scenarios with optically thick particulate layers. Six stream radiances are accurate to the 0.25% level for clear sky situations, and 0.65% for the special cases; weighting functions for the 6 stream output are accurate to $\pm 2\%$ in all cases. We discuss the implications of these comparisons regarding the performance and accuracy of the radiative transfer forward model in the ozone profile retrieval context.
© 2002 Elsevier Science Ltd. All rights reserved.

Keywords: Discrete ordinates; Linearization; 4/6 stream; Ozone profile retrieval

* Corresponding author. Tel.: +1-617-496-7819; fax: +1-617-495-7389.
E-mail address: rspurr@cfa-harvard.edu (R.J.D. Spurr).

0022-4073/02/$ - see front matter © 2002 Elsevier Science Ltd. All rights reserved.
PII: S0022-4073(01)00246-1

1. Introduction

Monitoring of the earth's atmosphere is an essential requirement to the understanding of chemical and physical processes that maintain atmospheric balance. This is particularly important in view of perceived changes in the atmosphere's constituent distributions due to anthropogenic activity on the planet. Space-based instruments have the potential to deliver global and long-term measurements of the vertical and horizontal distributions of atmospheric constituents, from the determination of column abundances and profile concentrations of ozone and other trace species, to the evaluation of aerosol and cloud properties and distributions. Ozone is the most important trace species, and in this work we will be concerned with the forward model component of ozone profile retrieval algorithms based on satellite nadir earthshine measurements in the UV part of the spectrum.

The global ozone monitoring experiment (GOME) nadir viewing spectrometer on board the ESA ERS-2 satellite (launched April 1995) takes earthshine measurements in the UV, visible and near infrared; it has a spectral range of 240–790 nm, with a moderate spectral resolution of 0.2–0.4 nm [1]. An improved version of the GOME instrument, GOME-2, will fly on the first three METOP satellites [2]. The operational period of these platforms is 15 years, and this offers a unique opportunity to obtain a long-term, global ozone record. Other instruments with similar measurement capabilities to GOME and GOME-2 include SCIAMACHY [3] on the ENVISAT platform (launch Spring 2002) and OMI [4] on EOS-AURA (launch 2003). GOME and SCIAMACHY have maximum swaths of 960 and 1000 km respectively, with a maximum off-nadir scan angle at the satellite of $\simeq 32^{\circ}$. OMI (swath 2600 km) and GOME-2 (maximum swath 1920 km) have wide-angle nadir viewing scenarios, and sphericity effects will be important for these instruments.

The first operational ozone profile retrieval algorithm from UV nadir measurements was developed for the BUV, SBUV, SBUV/2 and SSBUV experiments [5]. Ozone profile retrieval algorithms for GOME have been reported in the literature [6–9]. The potential of GOME-type instruments to deliver ozone profiles (Level 2 data) with the temporal and geographical sampling of the corresponding earthshine measurements (Level 1 data) can only be exploited if the retrieval process is fast enough to keep up with the data rate using the best available computer resources. It is highly desirable to develop algorithms which are as efficient as possible, and to find the right balance between accuracy and speed.

The ozone profile algorithm requires repeated calculations of simulated radiances and Jacobian matrices of radiance derivatives with respect to retrieval parameters (weighting functions). A tremendous saving in time is achieved with a radiative transfer (RT) model that is capable of delivering both these quantities simultaneously, without the need for cumbersome finite-difference approximations to the weighting functions obtained by repeated calls to a radiance-only radiative transfer model. The linearized discrete ordinate radiative transfer (LIDORT) model [10,11] has been designed with this purpose in mind; it is able to generate all weighting functions simultaneously to the same degree of accuracy as that pertaining for the radiance. Furthermore, the derivation of weighting functions is analytic, depending on an explicit differentiation of the complete RT solution.

In the discrete ordinate method, multiple scatter integrals over the polar viewing angle are replaced by quadrature sums defined by a set of Gauss–Legendre abscissae and weights (streams). The accuracy of the radiance at TOA computed with the discrete ordinate model is mainly determined by the number of streams. A high level of accuracy can be achieved for a sufficient number of streams; this is especially true for a strongly anisotropic medium. Taking only four or six streams therefore

involves some loss of accuracy. For atmospheres with aerosol scattering, we use the standard delta-M scaling [12] to separate the forward scatter peak as a delta-function and truncate the phase function; this process requires an initial scaling of the single scattering albedos and optical thicknesses before the model is executed. For a low number of streams, the single scatter contributions to the upwelling TOA radiance are not well treated in the delta-M approximation. To remedy this, we use the Nakajima–Tanaka (NT) correction procedure [13], which replaces the single scatter terms with analytical results computed for exact phase functions.

Analytic 4 stream solutions were derived by Liou [14] for the azimuth-independent component of the radiance field (this is sufficient to obtain heating rates and fluxes). In this work we extend the analytic 4 stream solution to cover the azimuth dependence of the radiation field, and we develop corresponding analytic expressions for the 6 stream model. A reduction in order by a factor of two is possible when solving for the homogeneous and particular solutions of the discrete ordinate RTE. These solutions can then be developed analytically for the low-stream cases, thereby avoiding numerical procedures (eigenproblem analysis and linear algebra systems) otherwise required for a higher number of streams. In a multi-layer atmosphere, a set of boundary conditions is required to complete the determination of the radiance; the resulting boundary value problem is a sparse linear algebra system. In solving this system, the time-consuming matrix inversion step is greatly speeded up with 4 and 6 stream approximations (speed varies with the square of the number of streams).

The determination of weighting functions for these models is carried out by explicit analytic differentation of the complete radiance field; this is the method adopted in the general LIDORT treatment [11]. Derivatives of the TOA radiance are taken with respect to the input optical properties that control the radiance calculation (total optical thickness, total single scattering albedo and phase function moments). Weighting functions with respect to *atmospheric* parameters then follow once we establish the dependence of the total optical input variables on these atmospheric parameters. We look at this dependence for parameters such as ozone profile volume mixing ratio, temperature, aerosol optical thickness and single scattering albedo. In addition, we derive weighting functions with respect to parameters such as the asymmetry factor which characterize the angular distribution of the phase function; such quantities are important for retrievals of aerosol optical properties.

In common with the general LIDORT treatment [11], the 4/6 stream models will use the pseudo-spherical approximation, in which the attenuation of the direct solar beam is computed accurately in spherical shell geometry, but all scattered light (with the exception of the NT-corrected single scatter terms) is treated for a plane-parallel atmosphere. The advantage of this approximation is that the power and speed of the plane-parallel scattering formalism can be retained without the need to call a greatly more complex and time-consuming full-spherical radiative transfer model. It has been shown [15,16] that the pseudo-spherical treatment is adequate for solar zenith angles up to 90° provided the line-of-sight is reasonably close ($\simeq 20$–25° or less) to the nadir. Fig. 1(a) illustrates the viewing geometry for this case; all scattering takes place along the nadir AC.

For wide-angle off-nadir viewing it is necessary to allow for sphericity effects; the situation is shown in Fig. 1(b), where scattering takes place along path AB instead of the vertical AC. To determine the upwelling radiation field at B, we obtain accurate single scatter contributions at points V_n along AB, taking curved geometry into account for all solar paths as well as path AB itself. Multiple scatter contributions at points V_n are determined from the pseudo-spherical models with the appropriate geometry for these points; the complete solution at B is found by using a layer-by-layer integrated source function method. Single scatter contributions will be NT-corrected. The multiple

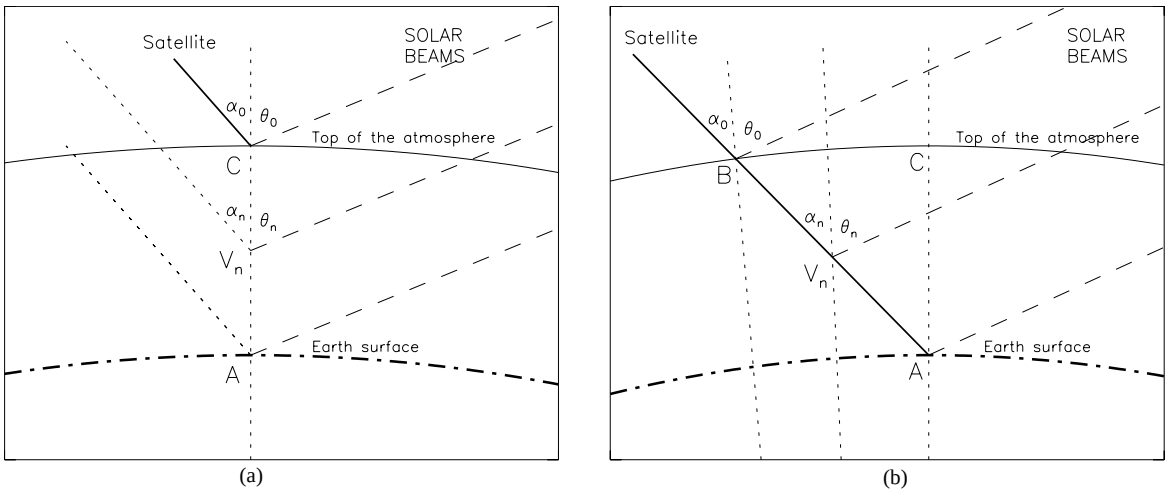

Fig. 1. (a) Geometry for the regular pseudo-spherical computation of backscatter radiation; (b) geometry for the sphericity correction.

scatter contributions vary smoothly with the small changes in viewing geometry from A to B, and we demonstrate that interpolation based on two or three computations is sufficiently accurate. We use the term *sphericity correction* for the calculation of TOA radiance. The correction was developed for LIDORT in [11], and a similar procedure has been applied to the finite difference GOMETRAN model [17]. Studies have shown that this sort of sphericity correction applied to pseudo-spherical RT models gives a very good approximation to the radiance computed using a full-spherical model [16].

The first three sections of the paper deal with theoretical aspects. In Section 2 on discrete ordinate theory, we concentrate in particular on the reduction in order which allows the analytic solutions to be written down in the 4 and 6 stream cases. In Section 3, we carry out an explicit differentiation of all aspects of the discrete ordinate solution in order to obtain analytically derived weighting functions, again focusing on the low-stream cases. This differentiation process is the *linearization* of the forward model. In Section 4 we discuss the various correction procedures used to enhance the model accuracy for a low number of streams (delta-M, NT correction and sphericity correction).

In Section 5 we examine the accuracy of the 4/6 stream models by carrying out extensive comparisons with 20 stream output from the LIDORT model. We look at a wavelength range of 299–335 nm covering that part of the UV spectrum wherein multiple scattering effects must be included in the RT modeling. Ozone is the only absorber. We look at three atmospheric situations: a reference clear sky atmosphere with scattering by molecules and background aerosol distributions; the same atmosphere but containing a tropospheric cloud layer of variable optical thickness; and thirdly, the reference atmosphere with one layer containing an optically thick scattering medium such as desert dust. We consider also the dependence on surface albedo (assumed Lambertian). A wide range of viewing geometries will be considered, appropriate to the nadir viewing conditions encountered by the two GOME instruments, SCIAMACHY and OMI. Section 5.2 examines the efficacy of the NT single scatter correction, while Section 5.3 looks at the effect of the sphericity

correction. The main conclusions from this study are summarized in Section 6, which also contains a discussion on the consequences regarding performance and accuracy trade-off in an operational ozone profile retrieval context.

2. Discrete ordinate theory with analytic 4/6 stream solutions

We derive homogeneous and particular solutions for the general discrete-ordinate model, noting especially the factor of 2 reduction that allows analytic solutions to be written down for the 4/6 stream cases. The equation of radiative transfer is solved for a vertically inhomogeneous atmosphere by assuming a division into a number of optically uniform adjacent sub-layers. The RTE is first solved for each of these layers, and this is followed by the application of boundary conditions to match the radiation field at the layer interfaces. The atmosphere is illuminated by a downward-directed parallel beam of sunlight entering at the top of the atmosphere. The diffuse radiation field (excluding the attenuated direct beam) is determined for the whole atmosphere. Since we are dealing with the UV/visible part of the spectrum, thermal emission is not taken into account. The effect of the sphericity of the atmosphere on the direct beam attenuation is accounted for using the pseudo-spherical "average secant" approximation [11,15]. Polarization is not considered.

The input optical parameters for the complete problem are for each layer p, where $p = 1, \ldots, P$: $\Delta\tau_p = \tau_p - \tau_{p-1}$, the layer optical thickness and the quantity $\beta^*_{l,p} \equiv \omega_p \beta_{l,p}$, where ω_p is the single scattering albedo (ratio of the *total* scattering and extinction coefficients), and $\beta_{l,p}$ are the phase function Legendre expansion moments (indexed by l). We note that ω_p and $\beta_{l,p}$ only enter the discrete ordinate solution through the product $\beta^*_{l,p}$. The optical depth for extinction τ acts as the vertical co-ordinate, with $\tau = \tau_p$ at the bottom of layer p; τ is zero at the top of the atmosphere. These parameters are computed from:

$$\Delta\tau_p = \sum_{\varsigma} \Delta\tau_{\mathrm{s},p,\varsigma} + \sum_{\alpha} \Delta\tau_{\mathrm{a},p,\alpha}, \tag{1}$$

$$\beta^*_{l,p} = \frac{1}{\Delta\tau_p} \sum_{\varsigma} \Delta\tau_{\mathrm{s},p,\varsigma} \beta_{l,p,\varsigma}. \tag{2}$$

Here $\Delta\tau_{\mathrm{s},p,\varsigma}$ is the contribution of scatterer ς to the layer optical thickness for scattering, $\Delta\tau_{\mathrm{a},p,\alpha}$ is the contribution of absorber α to the layer optical thickness for absorption, and $\Delta\tau_p$ is the total layer optical thickness for extinction. A realistic atmosphere contains air molecules and various kinds of aerosols as the scattering agents. Each scatterer is further specified by its phase function moments $\beta_{l,p,\varsigma}$ in (2).

We start with the equation of radiative transfer for layer p:

$$\mu \frac{\mathrm{d}I(\tau,\mu,\phi)}{\mathrm{d}\tau} = I(\tau,\mu,\phi) - J_p(\tau,\mu,\phi), \tag{3}$$

$$J_p(\tau,\mu,\phi) = \frac{\omega_p}{4\pi} \int_{-1}^{1} \mathrm{d}\mu' \int_{0}^{2\pi} \mathrm{d}\phi' \mathscr{P}_p(\mu,\phi;\mu',\phi') I(\tau,\mu',\phi') + \frac{\omega_p}{4\pi} \mathscr{P}_p(\mu,\phi;-\mu_0,\phi_0) F_p \mathrm{e}^{-\lambda_p \tau}. \tag{4}$$

Here, $I(\tau,\mu,\phi)$ is the diffuse radiance (excluding the direct solar beam) in direction (μ,ϕ) and at optical depth τ; μ is the cosine of the polar angle, ϕ the azimuthal angle. $\mathscr{P}_p(\mu,\phi;\mu',\phi')=\mathscr{P}_p(\mu_s)$ is the phase function for scattering, which depends on scattering angle θ_s, with $\mu_s=\cos\theta_s$. Primes denote the direction of the outgoing beam. The source function J_p represents the sources of diffuse radiation, namely scattered diffuse light and scattered light from the direct solar beam.

The solar beam enters the top of the atmosphere (TOA) in direction $(-\theta_0,\phi_0)$, $\mu_0=\cos\theta_0$. For the plane-parallel case F_p equals F_0, the solar irradiance at TOA and $\lambda_p=1/\mu_0$. In the pseudo-spherical treatment, F_p and λ_p are adjusted to account for the reduced path of the direct beam. In the average secant approximation, their values are determined by the requirement that the exponential dependence of the direct beam attenuation is exact at layer boundaries:

$$\lambda_p=\frac{\tilde{\tau}_p-\tilde{\tau}_{p-1}}{\Delta\tau_p}, \tag{5}$$

$$F_p=F_0\exp(-\tilde{\tau}_p+\lambda_p\tau_p) \tag{6}$$

with $\tilde{\tau}_p$ the slant optical depth and τ_p the vertical optical depth from TOA to the bottom of layer p. The slant optical depth has to be calculated by ray-tracing for a refractive atmosphere, which should be used for solar zenith angles larger than 85° [11]. In general we can write the slant optical depth as

$$\tilde{\tau}_p=\sum_{q=1}^{p}s_{pq}\Delta\tau_q. \tag{7}$$

This definition introduces the coefficients s_{pq} which characterize the deviation from plane-parallel geometry. In the latter case, all these coefficients are equal to $1/\mu_0$. Without refraction, straightforward goniometry results in the so-called Chapman function [15]:

$$s_{pq}=\frac{\sqrt{z_{q-1}^2-z_p^2\sin^2\theta_0}-\sqrt{z_q^2-z_p^2\sin^2\theta_0}}{z_{q-1}-z_q} \tag{8}$$

with z_p the altitude of the bottom of layer p relative to the center of the Earth. More precise parameterizations of the direct beam attenuation have been considered in [11]. Note that $1/\lambda_p$ is merely a parameter that describes the dependence of the attenuation on vertical optical depth; in general for the pseudo-spherical treatment, it is not equal to the cosine of the solar zenith angle. Note also that μ_0 is retained in the phase function in (3); this is strictly speaking only correct for an atmosphere without refraction.

To solve (3), the radiance field is expanded in a Fourier cosine series in the azimuth angle, and the phase function is expanded in a series of $2N$ ordinary Legendre polynomials P_l:

$$I(\tau,\mu,\phi)=\sum_{m=0}^{2N-1}I^m(\tau,\mu)\cos m(\phi_0-\phi), \tag{9}$$

$$\mathscr{P}_p(\mu_s)=\sum_{l=0}^{2N-1}\beta_l P_l(\mu_s)\quad\text{with }\beta_{l,p}=\frac{2l+1}{2}\int_{-1}^{1}P_l(\mu_s)\mathscr{P}_p(\mu_s)\,\mathrm{d}\mu_s. \tag{10}$$

Using the addition theorem for Legendre polynomials and performing the integration over the azimuth angle, we get $2N$ decoupled equations for each successive Fourier component $m = 0, \ldots, 2N-1$:

$$\mu \frac{\mathrm{d}I^m}{\mathrm{d}\tau} = I^m - \int_{-1}^{1} D_p^m(\mu, \mu') I^m(\tau, \mu')\, \mathrm{d}\mu' - Q_p^m(\mu) F_p \mathrm{e}^{-\lambda_p \tau}, \tag{11}$$

where

$$D_p^m(\mu, \mu') = \frac{1}{2} \sum_{l=m}^{2N-1} \omega_p \beta_{l,p} Y_l^m(\mu) Y_l^m(\mu') = \frac{1}{2} \sum_{l=m}^{2N-1} \beta_{l,p}^* Y_l^m(\mu) Y_l^m(\mu'), \tag{12}$$

$$Q_p^m(\mu) = \frac{1}{2\pi}(2 - \delta_{m0}) D_p^m(\mu, -\mu_0). \tag{13}$$

Y_l^m are the normalized associated Legendre polynomials. In the interests of clarity, we omit the Fourier superscripts m and the layer index p in the following, re-introducing these indices prior to consideration of the boundary value problem.

In the Nth-order discrete-ordinates approximation, the integral in (11) is approximated by a summation using Gauss–Legendre quadrature over the two half spaces separately. Each quadrature has N points, with abscissae μ_i and weights a_i for $i = 1, \ldots, N$ in the positive half-space, and corresponding values $\mu_{-i} = -\mu_i$ and $a_{-i} = a_i$ in the other half-space. Defining $M_i^+ = I_i^+ + I_i^-$ and $M_i^- = I_i^+ - I_i^-$, with $I_i^\pm = I(\tau, \pm\mu_i)$, we can write from (11):

$$\frac{\mathrm{d}M_i^+}{\mathrm{d}\tau} = -\sum_{j=1}^{N} (\zeta_{ij} - \eta_{ij}) M_j^- - \frac{1}{\mu_i}(Q_i^+ - Q_i^-) F \mathrm{e}^{-\lambda\tau}, \tag{14}$$

$$\frac{\mathrm{d}M_i^-}{\mathrm{d}\tau} = -\sum_{j=1}^{N} (\zeta_{ij} + \eta_{ij}) M_j^+ - \frac{1}{\mu_i}(Q_i^+ + Q_i^-) F \mathrm{e}^{-\lambda\tau}, \tag{15}$$

where $Q_i^\pm = Q(\pm\mu_i)$. The two $N \times N$ matrices $\boldsymbol{\zeta}$ and $\boldsymbol{\eta}$ are given by

$$\zeta_{ij} = \frac{1}{\mu_i}(a_i D_{ij}^+ - \delta_{ij}), \quad \eta_{ij} = \frac{1}{\mu_i} a_i D_{ij}^-, \tag{16}$$

with $D_{ij}^\pm = D(\mu_i, \pm\mu_j)$. A single equation for M_i^- can be obtained from (14) and (15):

$$\frac{\mathrm{d}^2 M_i^-}{\mathrm{d}\tau^2} = \sum_{j=1}^{N} \Gamma_{ij} M_j^- + d_i F \mathrm{e}^{-\lambda\tau}, \tag{17}$$

where

$$\Gamma_{ij} = \sum_{k=1}^{N} (\zeta_{ik} + \eta_{ik})(\zeta_{kj} - \eta_{kj}), \tag{18}$$

$$d_i = \frac{1}{\mu_i} \lambda (Q_i^+ + Q_i^-) + \frac{1}{\mu_i} \sum_{j=1}^{N} (\zeta_{ij} + \eta_{ij})(Q_i^+ - Q_i^-). \tag{19}$$

The general solution to (17) may be written:

$$M_i^- = \tilde{M}_i^- + W_i^- F \mathrm{e}^{-\lambda\tau}, \tag{20}$$

with $\tilde{M}_i^-$ the general solution to the homogeneous part of (17). The latter admits solutions of the form $\tilde{M}_i^- = Y_i^- \mathrm{e}^{-k\tau}$, and this leads to the eigenproblem:

$$\sum_{j=1}^{N} \Gamma_{ij} Y_j^- = \gamma Y_i^-, \tag{21}$$

where $\gamma = k^2$. Denote the N eigenvectors and eigenvalues of this system (21) as: $\{Y_{ij}^-, \gamma_j\}$, $j = 1, \ldots, N$. Note that since Γ_{ij} is a Hermitian matrix, all eigenvalues are real. In the general case, we solve the system using a standard package such as module DGEEV from the LAPACK numerical suite [18]. However, analytical solutions can be found for the 4 and 6 stream cases $N = 2$ and 3, respectively (see below). The eigenvector normalization may be chosen freely; for the 4 and 6 stream analytical eigensolutions, we have set the diagonal elements of the eigenvector matrix to unity.

4 stream eigensolutions:

$$\gamma_{1,2} = \tfrac{1}{2}(\Gamma_{11} + \Gamma_{22}) \pm \tfrac{1}{2}\sqrt{(\Gamma_{11} - \Gamma_{22})^2 + 4\Gamma_{21}\Gamma_{12}}, \tag{22}$$

$$Y_{11}^- = 1, \quad Y_{22}^- = 1, \quad Y_{21}^- = \frac{\Gamma_{21}}{\gamma_1 - \Gamma_{22}}, \quad Y_{12}^- = \frac{\Gamma_{12}}{\gamma_2 - \Gamma_{11}}. \tag{23}$$

4 stream particular solutions:

$$W_1^- = \frac{\Gamma_{12} d_2 + (\lambda^2 - \Gamma_{22}) d_1}{\Psi}, \quad W_2^- = \frac{\Gamma_{21} d_1 + (\lambda^2 - \Gamma_{11}) d_2}{\Psi}, \tag{24}$$

$$\Psi = \lambda^4 - (\Gamma_{11} + \Gamma_{22})\lambda^2 + \Gamma_{11}\Gamma_{22} - \Gamma_{12}\Gamma_{21}. \tag{25}$$

6 stream eigensolutions:

$$0 = \gamma^3 - A\gamma^2 + B\gamma + C,$$

(eigenvalues γ_j, $j = 1, 2, 3$ are real and positive roots of cubic equation)

$$A = \mathrm{Trace}(\boldsymbol{\Gamma}),$$

$$B = \Gamma_{11}\Gamma_{22} + \Gamma_{11}\Gamma_{33} + \Gamma_{22}\Gamma_{33} - \Gamma_{23}\Gamma_{32} - \Gamma_{13}\Gamma_{31} - \Gamma_{12}\Gamma_{21},$$

$$C = \mathrm{Det}(\boldsymbol{\Gamma}).$$

$$\frac{Y_{2j}^-}{Y_{1j}^-} = \frac{\Gamma_{13}\Gamma_{21} - \Gamma_{23}(\Gamma_{11} - \gamma_j)}{\Gamma_{23}\Gamma_{12} - \Gamma_{13}(\Gamma_{22} - \gamma_j)}, \quad \frac{Y_{3j}^-}{Y_{1j}^-} = \frac{\Gamma_{12}\Gamma_{31} - \Gamma_{32}(\Gamma_{11} - \gamma_j)}{\Gamma_{13}\Gamma_{32} - \Gamma_{12}(\Gamma_{33} - \gamma_j)},$$

$$Y_{jj}^- = 1 \quad \text{for } j = 1, 2, 3. \quad \text{(Normalization)}$$

6 stream particular solutions:

$$W_1^- = \frac{\mathrm{Det}(\boldsymbol{M}_{(1)})}{\mathrm{Det}(\boldsymbol{M})}, \quad W_2^- = \frac{\mathrm{Det}(\boldsymbol{M}_{(2)})}{\mathrm{Det}(\boldsymbol{M})},$$

$$W_3^- = \frac{-d_1 - (\Gamma_{11} - \lambda^2)W_1^- - \Gamma_{12}W_2^-}{\Gamma_{13}},$$

$$M_{ij} = \lambda^2\delta_{ij} - \Gamma_{ij},$$

$$\{M_{ij}\}_{(k)} = \delta_{jk}d_i + (1 - \delta_{jk})M_{ij} \quad \text{(matrix } \boldsymbol{M} \text{ with column } k \text{ replaced by vector } \boldsymbol{d}\text{)}$$

The inhomogeneous or particular part of the solution can be found by substitution of (20) into (17):

$$\lambda^2 W_i^- = \sum_{j=1}^{N} \Gamma_{ij}W_j^- + d_i \tag{26}$$

and solving for W_i^-. For the general N-stream case, this linear system of order N can be solved by standard numerical techniques. For the 4 and 6 stream cases ($N = 2$ and 3), analytical solutions are written above.

Bringing the two parts together, the general solution to (17) is then:

$$M_i^- = \sum_{j=1}^{N} \{\tilde{L}_j^+ Y_{ij}^- \mathrm{e}^{-k_j\tau} + \tilde{L}_j^- Y_{ij}^- \mathrm{e}^{+k_j\tau}\} + W_i^- F\mathrm{e}^{-\lambda\tau}, \tag{27}$$

where $\tilde{L}_j^+$ and $\tilde{L}_j^-$ are the $2N$ constants of integration, and $k_j = +\sqrt{\gamma_j}$. From (14) we have for M_i^+:

$$M_i^+ = \sum_{j=1}^{N} \{\tilde{L}_j^+ Y_{ij}^+ \mathrm{e}^{-k_j\tau} - \tilde{L}_j^- Y_{ij}^- \mathrm{e}^{+k_j\tau}\} + W_i^+ F\mathrm{e}^{-\lambda\tau} \tag{28}$$

with:

$$Y_{ij}^+ = \frac{1}{k_j}\sum_{k=1}^{N} (\zeta_{ik} - \eta_{ik})Y_{kj}^-, \tag{29}$$

$$W_i^+ = \frac{1}{\lambda}\sum_{j=1}^{N} (\zeta_{ij} - \eta_{ij})W_j^- + \frac{1}{\lambda\mu_i}(Q_i^+ - Q_i^-). \tag{30}$$

Retention of the inhomogeneous terms in (17) shows clearly that the reduction in dimension applies to the particular solution as well as to the homogeneous solutions. Returning to I^+ and I^- and re-introducing the Fourier and layer indices, we can write down the solution for a Fourier component of the radiance at the Gaussian polar angles for any optical depth in a specific layer p:

$$I_p^m(\tau, \mu_i) = \sum_{j=1}^{N} \{L_{j,p}^+ X_{ij,p}^+ \mathrm{e}^{-k_{j,p}(\tau - \tau_{p-1})} + L_{j,p}^- X_{ij,p}^- \mathrm{e}^{-k_{j,p}(\tau_p - \tau)}\} + Z_{i,p}F_p\mathrm{e}^{-\lambda\tau}, \tag{31}$$

$\forall i \in \{\pm 1, \ldots, \pm N\}$; $L^+_{j,p}$ and $L^-_{j,p}$ are integration constants. We have defined:

$$X^+_{ij,p} = \tfrac{1}{2}(Y^+_{ij,p} + Y^-_{ij,p}), \quad X^+_{-ij,p} = \tfrac{1}{2}(Y^+_{ij,p} - Y^-_{ij,p}), \tag{32}$$

$$X^-_{ij,p} = X^+_{-ij,p}, \tag{33}$$

$$Z_{i,p} = \tfrac{1}{2}(W^+_{i,p} + W^-_{i,p}), \quad Z_{-i,p} = \tfrac{1}{2}(W^+_{i,p} - W^-_{i,p}). \tag{34}$$

Exponential arguments in (31) have been written as optical depth differences; this safeguards the numerical stability of the solution [19,20].

The integration constants follow from a set of three boundary conditions. These are (1) radiance values at the $P-1$ layer interfaces are continuous at the Gaussian angles; (2) at the top of the atmosphere the downwelling diffuse radiance is zero; and (3) at the bottom of the atmosphere, upwelling and downwelling radiances are linked by a suitable reflectance relation. These conditions provide a total of $2N \times P$ linear equations to determine the integration constants. The layer interface boundary conditions read:

$$\sum_{j=1}^{N} \{L^+_{j,p-1} X^+_{ij,p-1} \Theta_{j,p-1} + L^-_{j,p-1} X^-_{ij,p-1} - L^+_{j,p} X^+_{ij,p} - L^-_{j,p} X^-_{ij,p} \Theta_{j,p}\}$$

$$= (Z_{i,p} - Z_{i,p-1}) F_0 \tilde{T}_p, \tag{35}$$

where $i = -N, \ldots, N$ $(i \neq 0)$ and $p = 2, \ldots, P$. The following definitions have been used:

$$\Theta_{j,p} = \mathrm{e}^{-k_{j,p} \Delta\tau_p}, \tag{36}$$

$$\tilde{T}_p = \mathrm{e}^{-\tilde{\tau}_p}. \tag{37}$$

The boundary condition at the top of the atmosphere reads:

$$\sum_{j=1}^{N} \{L^+_{j,1} X^+_{ij,1} + L^-_{j,1} X^-_{ij,1} \Theta_{j,1}\} = -Z_{i,1} F_0, \tag{38}$$

where $i = -N, \ldots, 0$. For the boundary condition at the bottom of the atmosphere (BOA) we limit ourselves to the Lambertian condition, with albedo A. For $m = 0$, we have:

$$\sum_{j=1}^{N} \{L^+_{j,P} \hat{X}^+_{ij,P} \Theta_{j,P} + L^-_{j,P} \hat{X}^-_{ij,P}\} = -\hat{Z}_{i,P} F_0 \tilde{T}_P + \frac{A}{\pi} \mu_0 F_0 \tilde{T}_P, \tag{39}$$

which holds $\forall i \in \{1, \ldots, N\}$. For $m \neq 0$, (39) still applies, but now $A = 0$. We have introduced:

$$\hat{X}^{\pm}_{ij,P} = X^{\pm}_{ij,P} - 2A \sum_{k=-N}^{-1} a_k \mu_{-k} X^{\pm}_{kj,P}, \tag{40}$$

$$\hat{Z}_{i,P} = Z^{\pm}_{i,P} - 2A \sum_{k=-N}^{-1} a_k \mu_{-k} Z_{k,P}. \tag{41}$$

This linear system for $L^{\pm}_{i,p}$ is sparse, in the sense that the matrix only contains non-zero terms in a band along the diagonal. The LIDORT code uses a special LU-decomposition routine from LAPACK [18] that makes use of this sparseness and thereby saves considerably on the number of floating point operations. For the 4/6 stream cases this computation step is the only one where a standard numerical package has to be used. Further discussion on these boundary conditions may be found in [10], where in particular, the surface boundary condition has been generalized to cover a bidirectional reflectance condition, and extended to include surface thermal emission. Although processing time for the overall radiance and weighting function computation is dominated by this numerical step, considerable savings are apparent with a small number of streams. Assuming floating-point operations in this step vary with N^2 for the radiance, the 4 stream algorithm is 25 times faster than a 20 stream calculation.

The discrete-ordinate solution gives radiance at Gaussian angles and at every optical depth in the atmosphere. However, the viewing direction does not usually coincide with one of the Gaussian angles; in this case some kind of interpolation in polar angle is desired. This *post processing* step can be done "smartly" by substituting the discrete ordinate solution at the Gaussian streams in the multiple scatter integrals in the original RTE, and integrating the latter. This procedure is known as source function integration [21,20]. The formal solution to (11) can be written:

$$I^m(0,\mu) = \mathscr{B}^m(\mu)\mathrm{e}^{-\tau_P/\mu} + \frac{1}{\mu}\sum_{p=1}^{P}\int_{\tau_p}^{\tau_{p-1}} J^m(\tau',\mu)\mathrm{e}^{-\tau'/\mu}\,\mathrm{d}\tau', \tag{42}$$

where $\mathscr{B}^m(\mu) \equiv I^m(\tau_P,\mu)$ is the BOA upwelling radiance at the surface, J^m is given by the last two terms on the RHS of (11), and μ is the cosine of the desired viewing angle. Replacing the integration over polar angle by a quadrature sum and using the discrete ordinate solutions from (31), we get:

$$I^m(0,\mu) = \mathscr{B}^m(\mu)T_P(\mu) + \sum_{p=1}^{P} T_{p-1}(\mu)\Lambda^m_p(\mu). \tag{43}$$

Transmittance along direction μ is simply $T_p(\mu)=\exp(-\tau_p/\mu)$ and the *layer integrated source terms* $\Lambda^m_p(\mu)$ consist of contributions $\Lambda^m_{p,(\mathrm{ms})}(\mu)$ from multiple scattered light and terms $\Lambda^m_{p,(\mathrm{ss})}(\mu)$ from atmospheric single scattering. We have:

$$\Lambda^m_p(\mu) = \Lambda^m_{p,(\mathrm{ms})}(\mu) + \Lambda^m_{p,(\mathrm{ss})}(\mu), \tag{44}$$

where

$$\Lambda^m_{p,(\mathrm{ms})}(\mu) = \sum_{j=1}^{N}\{L^+_{j,p}X^+_{j,p}(\mu)E^+_{j,p}(\mu) + L^-_{j,p}X^-_{j,p}(\mu)E^-_{j,p}(\mu)\} + Z_p(\mu)F_0E^0_p(\mu), \tag{45}$$

$$\Lambda^m_{p,(\mathrm{ss})}(\mu) = Q_p(\mu)F_0E^0_p(\mu) \tag{46}$$

with the following set of definitions:

$$X^{\pm}_{j,p}(\mu) = \frac{1}{2}\sum_{i=-N^{\dagger}}^{N} a_i D_p(\mu,\mu_i)X^{\pm}_{ij,p}, \tag{47}$$

$$Z_p(\mu) = \frac{1}{2} \sum_{i=-N^{1/2}}^{N} a_i D_p(\mu, \mu_i) Z_{i,p}, \tag{48}$$

$$E^+_{j,p}(\mu) = \frac{1 - t_p(\mu)\Theta_{j,p}}{1 + \mu k_{j,p}}, \tag{49}$$

$$E^-_{j,p}(\mu) = \frac{\Theta_{j,p} - t_p(\mu)}{1 - \mu k_{j,p}}, \tag{50}$$

$$E^0_p(\mu) = \frac{1}{1 + \mu\lambda_p}(\tilde{T}_{p-1} - \tilde{T}_p t_p(\mu)), \tag{51}$$

$$t_p(\mu) = \exp(-\Delta\tau_p/\mu). \tag{52}$$

The symbol indicates exclusion of the $i=0$ term from the summation. For a plane-parallel atmosphere, we use the appropriate particular solutions $Z_{i,p}$ in (48) and replace the average secant λ_p in (51) with the value μ_0^{-1}. Assuming a Lambertian surface with albedo A, the BOA upwelling radiance $\mathscr{B}^m(\mu)$ in (43) may be written (for Fourier component $m = 0$):

$$\mathscr{B}^m(\mu) = \frac{A\mu_0 F_0}{\pi}\tilde{T}_P + 2A \sum_{k=-N}^{-1} a_k \mu_{-k} \left[\sum_{j=1}^{N} \{ L^+_{j,P} X^+_{kj,P} \Theta_{j,P} + L^-_{j,P} X^-_{kj,P} \} + Z_{k,P} F_0 \tilde{T}_P \right]. \tag{53}$$

For $m \neq 0$, $\mathscr{B}^m(\mu) \equiv 0$ in the Lambertian case.

3. Linearized discrete ordinates: analytic weighting functions

3.1. Definitions and input optical parameter derivatives

In general, we define the weighting function from TOA radiance as follows:

$$K_x = \frac{\partial I(0, \mu)}{\partial x_p}, \tag{54}$$

where x_p is a parameter denoting some physical property in layer p. This parameter affects the TOA radiance through the optical parameters in layer p that are input for the radiative transport model: the product $\beta^*_{l,p}$ of the phase function moments and the single scattering albedo, and the layer optical thickness $\Delta\tau_p$. For a given retrieval application, we need to know in detail how these optical parameters depend on x_p. Specifically, the derivatives

$$\frac{\partial \Delta\tau_p}{\partial x_p} \quad \text{and} \quad \frac{\partial \beta^*_{l,p}}{\partial x_p} \tag{55}$$

have to be identified for all $l = 0, \ldots, 2N - 1$ (Note that $l = 0$ is included, since $\beta^*_{0,p} = \omega_p$ by definition). Before we determine the derivatives in (54) of the discrete ordinate solution outlined in

the previous section, we must establish the optical parameter derivatives in (55). This is an important first step in deriving weighting functions, and we illustrate this process for number of atmospheric parameters.

3.1.1. Layer column density of gas absorber α

The parameter in this case is defined as

$$x_p = \Delta C_{p,\alpha}, \tag{56}$$

where $C_{p,\alpha}$ is the column number density of gas α in layer p. The required partial derivatives are

$$\frac{\partial \beta^*_{l,p}}{\partial x_p} = -\frac{\beta^*_{l,p}}{\Delta\tau_p}\sigma_{p,\alpha}, \tag{57}$$

$$\frac{\partial \Delta\tau_p}{\partial x_p} = \sigma_{p,\alpha}, \tag{58}$$

where $\sigma_{p,\alpha}$ is the absorption cross section of gas α, and the layer index is retained since trace gas cross sections may possess temperature and pressure dependence. Note that both derivatives are linear in the cross sections, implying that the corresponding weighting functions are also linear in the cross sections. Hence, once the column density weighting functions have been calculated for gas α_1, corresponding weighting functions for any other gas α_2 may be found by scaling the original results by the cross section ratio $\sigma_{p,\alpha_2}/\sigma_{p,\alpha_1}$.

3.1.2. Temperature

The parameter in this case is temperature ϑ_p, which is assumed constant for the layer p. We take the layer to be specified by pressure levels (and not altitudes) at the upper and lower boundaries. When the layer is in local hydrostatic equilibrium with the acceleration due to gravity G assumed constant over the layer, then the column of air in the layer is simply equal to the pressure drop divided by G, and is independent of temperature. In this case temperature dependence is only manifest in the trace gas cross sections. For trace species α with cross section $\sigma_{p,\alpha}$, we find:

$$\frac{\partial \beta^*_{l,p}}{\partial x_p} = -\frac{\beta^*_{l,p}}{\Delta\tau_p}\Delta C_{p,\alpha}\frac{\partial \sigma_{p,\alpha}}{\partial x_p}, \tag{59}$$

$$\frac{\partial \Delta\tau_p}{\partial x_p} = \Delta C_{p,\alpha}\frac{\partial \sigma_{p,\alpha}}{\partial x_p}. \tag{60}$$

For O_3 absorption in the Huggins bands, the well-known Bass–Paur quadratic temperature parameterization [22] for the cross sections gives:

$$\sigma_{p,\alpha}(\vartheta_p) = \varsigma_0(1 + \vartheta_p\varsigma_1 + \vartheta_p^2\varsigma_2), \tag{61}$$

$$\frac{\partial \sigma_{p,\alpha}(\vartheta_p)}{\partial x_p} = \varsigma_0(\varsigma_1 + 2\vartheta_p\varsigma_2), \tag{62}$$

for ϑ_p in °C, and parameterization coefficients ς independent of atmospheric conditions. We remark that the weighting functions are now linear in the derivatives of the cross sections. Thus, if we have already calculated column density weighting functions for gas α, temperature weighting functions may be obtained by simply scaling these results with the ratio $(\partial\sigma_{p,\alpha}/\partial\vartheta_p)/\sigma_{p,\alpha}$.

3.1.3. Aerosol layer optical thickness

The parameter in this case is given by

$$x_p \equiv \Delta\tau_{\mathrm{s},p,\varsigma} + \Delta\tau_{\mathrm{a},p,\varsigma} = \omega_{p,\varsigma}^{-1}\Delta\tau_{\mathrm{s},p,\varsigma}, \tag{63}$$

where index ς labels a specific aerosol among the list of scatterers and absorbers. $\Delta\tau_{p,\varsigma}$ is the optical depth for extinction due to aerosol ς for layer p, and $\omega_{p,\varsigma}$ and $\Delta\tau_{\mathrm{s},p,\varsigma}$ are the single scattering albedo of the aerosol (assumed constant) and the layer optical depth for scattering respectively. The relevant partial derivatives are:

$$\frac{\partial\beta_{l,p}^*}{\partial x_p} = \frac{1}{\Delta\tau_p}(\omega_{p,\varsigma}^{-1}\beta_{l,p,\varsigma} - \beta_{l,p}^*), \tag{64}$$

$$\frac{\partial\Delta\tau_p}{\partial x_p} = 1. \tag{65}$$

3.1.4. Aerosol layer single scattering albedo

For layer p, the parameter is now:

$$x \equiv \omega_{p,\varsigma} = \frac{\Delta\tau_{\mathrm{s},p,\varsigma}}{\Delta\tau_{\mathrm{a},p,\varsigma} + \Delta\tau_{\mathrm{s},p,\varsigma}}. \tag{66}$$

Taking the layer aerosol optical thickness constant, we have:

$$\frac{\partial\beta_{l,p}^*}{\partial x} = \frac{1}{\Delta\tau_p}(\Delta\tau_{\mathrm{a},p,\varsigma} + \Delta\tau_{\mathrm{s},p,\varsigma})\beta_{l,p,\varsigma}, \tag{67}$$

$$\frac{\partial\Delta\tau_p}{\partial x} = 0. \tag{68}$$

3.1.5. Aerosol asymmetry parameter

In this case parameter x is the layer asymmetry parameter $g_{p,\varsigma}$, where ς again labels a specific aerosol. In this case we require the variation of the phase function moments $\beta_{l,p,\varsigma}$ with respect to x. In general, this would require an examination of the detailed microphysical scattering properties of the given aerosol. However, for a Henyey–Greenstein phase function, this variation is straightforward. Here, $\beta_{p,l,\varsigma} = (2l+1)g_{p,\varsigma}^l$ for $l = 0,\ldots,2N-1$, and hence

$$\frac{\partial\beta_{l,p}^*}{\partial x} = \frac{1}{\Delta\tau_p}\Delta\tau_{\mathrm{s},p,\varsigma}\, l(2l+1)g_{p,\varsigma}^{l-1}, \tag{69}$$

$$\frac{\partial\Delta\tau_p}{\partial x} = 0. \tag{70}$$

The first four examples are limited to variations of the *amount* of molecular and/or particulate constituents; in each case the angular distribution of the scattering is regarded as constant (the phase function moments $\beta_{l,p,\varsigma}$ have zero derivatives). The last example (asymmetry parameter) involved derivatives of the phase function moments, and this would be important for the retrieval of aerosol microphysical properties. In the present work, we are interested chiefly in layer column density weighting functions for the trace gas ozone, as these are essential for any ozone profile retrieval algorithm. However, additional weighting functions with respect to quantities such as aerosol optical thickness are also useful in such an algorithm, as they can be used to assess *process* errors in the ozone retrieval due to uncertainties in the assumed aerosol or temperature distributions [23].

Since TOA radiance is also a function of the surface albedo A, we can define an albedo weighting function $K_A = \partial I(0,\mu)/\partial A$ (in this work, we restrict ourselves to the Lambertian case; a more general bidirectional treatment can be found in [10,11]). Albedo derivatives are included in the next section.

3.2. Derivatives of the discrete ordinate solution with respect to x_p

In this section we present a (somewhat lengthy) exposition of the analytical determination of derivatives of the TOA-radiance with respect to layer parameters x_p and also with respect to albedo A. The procedure involves a term-by-term differentiation of the TOA radiance with repeated applications of the chain-rule of differentiation. The chain-rule differentiation terminates when we encounter an explicit dependency on one of the input parameters. At such a point we use the partial derivatives in (55) to finalize the procedure. The corresponding "end-point" equations are marked by a † symbol in the exposition; we will refer to these equations in the discussion on numerical implementation that follows. We start with differentiation of the Fourier sum (9):

$$\frac{\partial I(0,\mu,\phi)}{\partial x_p} = \sum_{m=0}^{2N-1} \frac{\partial I^m(0,\mu)}{\partial x_p} \cos m(\phi_0 - \phi), \tag{71}$$

$$\frac{\partial I(0,\mu,\phi)}{\partial A} = \sum_{m=0}^{2N-1} \frac{\partial I^m(0,\mu)}{\partial A} \cos m(\phi_0 - \phi). \tag{72}$$

The derivatives of the Fourier components can be obtained by differentiation of the post-processed discrete ordinate solution (43). We find:

$$\frac{\partial I(0,\mu)}{\partial x_p} = \frac{\partial I^m(\tau_P,\mu)}{\partial x_p} T_P(\mu) + I^m(\tau_P,\mu) \frac{\partial T_P(\mu)}{\partial x_p} + \sum_{q=1}^{P} \left\{ \frac{\partial T_{q-1}(\mu)}{\partial x_p} \Lambda_q(\mu) + T_{q-1}(\mu) \frac{\partial \Lambda_q(\mu)}{\partial x_p} \right\}, \tag{73}$$

$$\frac{\partial I^m(0,\mu)}{\partial A} = \frac{\partial I^m(\tau_P,\mu)}{\partial A} T_P(\mu) + \sum_{q=1}^{P} T_{q-1}(\mu) \frac{\partial \Lambda_q(\mu)}{\partial A}. \tag{74}$$

Note that layer source term $\Lambda_q(\mu)$ for layer q will not only depend on optical parameters from that layer, but also on optical parameters from layers p for $p \neq q$. The transmittance in direction μ from TOA to the bottom of layer p depends only on the optical thickness of layers above and including p:

$$\frac{\partial T_q(\mu)}{\partial \Delta\tau_p} = \begin{cases} -T_q(\mu)/\mu & \text{for } p \leqslant q, \\ 0 & \text{for } p > q. \end{cases} \tag{75}$$

Derivatives of the BOA upwelling radiance $\mathscr{B}^m(\mu)$ are determined from the surface boundary condition. For a Lambertian surface, we have for Fourier component $m=0$ (the index m is assumed):

$$\frac{\partial \mathscr{B}(\mu)}{\partial x_p} = 2A \sum_{k=-N}^{-1} a_k \mu_{-k} \left[\sum_{j=1}^{N} \left\{ \frac{\partial L^+_{j,P}}{\partial x_p} X^+_{kj,P} \Theta_{j,P} + L^+_{j,P} \frac{\partial X^+_{kj,P}}{\partial x_p} \Theta_{j,P} \delta_{pP} + L^+_{j,P} X^+_{kj,P} \frac{\partial \Theta_{j,P}}{\partial x_p} \delta_{pP} \right.\right.$$
$$\left.\left. + \frac{\partial L^-_{j,P}}{\partial x_p} X^-_{kj,P} + L^-_{j,P} \frac{\partial X^-_{kj,P}}{\partial x_p} \delta_{pP} \right\} - \frac{\partial Z_{k,P}}{\partial x_p} F_0 \tilde{T}_P - Z_{k,P} F_0 \frac{\partial \tilde{T}_P}{\partial x_p} \right] + \frac{A}{\pi} \mu_0 F_0 \frac{\partial \tilde{T}_P}{\partial x_p}, \tag{76}$$

$$\frac{\partial \mathscr{B}(\mu)}{\partial A} = \frac{\mathscr{B}(\mu)}{A} + 2A \sum_{k=-N}^{-1} a_k \mu_{-k} \left[\sum_{j=1}^{N} \left\{ \frac{\partial L^+_{j,P}}{\partial A} X^+_{kj,P} \Theta_{j,P} + \frac{\partial L^-_{j,P}}{\partial A} X^-_{kj,P} \right\} \right]. \tag{77}$$

From the definition of the layer transmittance $\Theta_{j,p}$ in Eq. (36) we have:

$$\frac{\partial \Theta_{j,p}}{\partial x_p} = -\left(k_{j,p} + \Delta\tau_p \frac{\partial k_{j,p}}{\partial x_p} \right) \Theta_{j,p} \frac{\partial \Delta\tau_p}{\partial x_p}. \tag{78}$$

For all layers $p > q$ the derivative of the pseudo-spherical transmittance $\tilde{T}_q$ is zero. For layers $p \leqslant q$ this derivative can be found using results (7) and (37):

$$\dagger \frac{\partial \tilde{T}_q}{\partial x_p} = \begin{cases} -s_{qp} \tilde{T}_q \frac{\partial \Delta\tau_P}{\partial x_p} & \text{for } p \leqslant q, \\ 0 & \text{for } p > q. \end{cases} \tag{79}$$

The derivatives of the layer source terms follow from the definition (44) and differentiation of (45) and (46). In the following expressions, we have differentiated total layer source terms, but the separation into multiple scatter and single scattering contributions is straightforward. We find:

$$\frac{\partial \Lambda^m_q(\mu)}{\partial x_p} = \sum_{j=1}^{N} \left\{ \frac{\partial L^+_{j,q}}{\partial x_p} X^+_{j,q}(\mu) E^+_{j,q}(\mu) + L^+_{j,q} \frac{\partial X^+_{j,q}(\mu)}{\partial x_q} \delta_{pq} E^+_{j,q}(\mu) + L^+_{j,q} X^+_{j,q}(\mu) \frac{\partial E^+_{j,q}(\mu)}{\partial x_q} \delta_{pq} \right.$$
$$\left. + \frac{\partial L^-_{j,q}}{\partial x_p} X^-_{j,q}(\mu) E^-_{j,q}(\mu) + L^-_{j,q} \frac{\partial X^-_{j,q}(\mu)}{\partial x_q} \delta_{pq} E^-_{j,q}(\mu) + L^-_{j,q} X^-_{j,q}(\mu) \frac{\partial E^-_{j,q}(\mu)}{\partial x_q} \delta_{pq} \right\}$$
$$+ \left[\frac{\partial Z_q(\mu)}{\partial x_p} + \frac{\partial Q_q(\tau,\mu)}{\partial x_q} \delta_{pq} \right] F_0 E^0_q(\mu) + [Z_q(\mu) + Q_q(\mu)] F_0 \frac{\partial E^0_q(\mu)}{\partial x_p}, \tag{80}$$

$$\frac{\partial \Lambda_q^m(\mu)}{\partial A} = \sum_{j=1}^{N} \left\{ \frac{\partial L_{j,q}^+}{\partial A} X_{j,q}^+(\mu) E_{j,q}^+(\mu) + \frac{\partial L_{j,q}^-}{\partial A} X_{j,q}^-(\mu) E_{j,q}^-(\mu) \right\}. \tag{81}$$

Some layer quantities depend only on the optical parameters of the layer in which they are defined; others have cross-layer derivatives. The eigenvalues, eigenvectors and the $E^{\pm}(\mu)$ terms in (49) and (50) have vanishing cross-layer derivatives. Furthermore, the eigen-quantities have no dependence on optical thickness. The $E^0(\mu)$ term in (51) defined for layer p depends on optical thicknesses of layers above p. The dependence of the particular solution in layer q on optical thickness values for layers $p \leqslant q$ is more subtle. This dependence is expressed through the average secant factor λ_q appropriate to the pseudo-spherical treatment of the direct beam source. The integration constants depend on all optical parameters in all layers because of the coupling implicit in the linear system defined by the set of boundary conditions. These dependencies will be clarified below, when we consider expressions for the various terms in (80) and (81).

Starting with $Q_p(\mu)$ from (13), we find:

$$\frac{\partial Q_p(\mu)}{\partial x_p} = \frac{1}{2\pi}(2 - \delta_{m0}) \frac{\partial D_p(\mu, -\mu_0)}{\partial x_p}. \tag{82}$$

We have also the cross-layer derivatives:

$$\frac{\partial \{E_q^0(\mu)\}}{\partial x_p} = -\frac{E_q^0(\mu)}{1 + \mu\lambda_q} \mu \frac{\partial \lambda_q}{\partial x_p} + \frac{1}{1 + \mu\lambda_q} \left[\frac{\partial \tilde{T}_{q-1}}{\partial x_p} - \frac{\partial \tilde{T}_q}{\partial x_p} t_q(\mu) - \tilde{T}_q \frac{\partial t_q(\mu)}{\partial x_q} \delta_{pq} \right] \tag{83}$$

with

$$\dagger \frac{\partial t_p(\mu)}{\partial x_p} = -\frac{1}{\mu} t_p(\mu) \frac{\partial \Delta\tau_P}{\partial x_p}. \tag{84}$$

Using (5) and (7) we can write:

$$\dagger \frac{\partial \lambda_q}{\partial x_p} = \begin{cases} \frac{s_{qp} - s_{q-1,p}}{\Delta\tau_q} \frac{\partial \Delta\tau_P}{\partial x_p} & \text{for } p < q, \\ \frac{s_{qq} - \lambda_q}{\Delta\tau_q} \frac{\partial \Delta\tau_P}{\partial x_p} & \text{for } p = q, \\ 0 & \text{for } p > q. \end{cases} \tag{85}$$

For a plane-parallel medium, $s_{pq} = \lambda_q = 1/\mu_0$ for all $p, q = 1, \ldots, P$, so that the cross-layer derivatives in (85) vanish in this case. Derivatives of the other two exponential functions $E^{\pm}(\mu)$ follow from straightforward differentiation using the definitions. We get:

$$\frac{\partial E_{j,p}^+}{\partial x_p} = -\frac{1}{1 + \mu k_{j,p}} \left\{ t_p(\mu) \frac{\partial \Theta_{j,p}}{\partial x_p} + \frac{\partial t_p(\mu)}{\partial x_p} \Theta_{j,p} + E_{j,p}^+ \mu \frac{\partial k_{j,p}}{\partial x_p} \right\}, \tag{86}$$

$$\frac{\partial E_{j,p}^-}{\partial x_p} = \frac{1}{1 - \mu k_{j,p}} \left\{ \frac{\partial \Theta_{j,p}}{\partial x_p} - \frac{\partial t_p(\mu)}{\partial x_p} + E_{j,p}^- \mu \frac{\partial k_{j,p}}{\partial x_p} \right\}. \tag{87}$$

Next we consider the derivatives of the eigenvectors, plus derivatives of the eigensolutions defined for user angles in (80):

$$\frac{\partial X^{\pm}_{j,p}(\mu)}{\partial x_p} = \frac{1}{2}\sum_{i=-N}\left\{ a_i \frac{\partial D_p(\mu,\mu_i)}{\partial x_p} X^{\pm}_{ij,p} + a_i D_p(\mu,\mu_i)\frac{\partial X^{\pm}_{ij,p}}{\partial x_p}\right\}, \tag{88}$$

$$\frac{\partial X^{\pm}_{ij,p}}{\partial x_p} = \frac{1}{2}\left(\frac{\partial Y^{+}_{ij,p}}{\partial x_p} \pm \frac{\partial Y^{-}_{ij,p}}{\partial x_p}\right) \tag{89}$$

and from (29) we find:

$$\frac{\partial Y^{+}_{ij,p}}{\partial x_p} = -Y^{+}_{ij,p}\frac{1}{k_{j,p}}\frac{\partial k_{j,p}}{\partial x_p} + \frac{1}{k_{j,p}}\sum_{k=1}^{N}\left\{\left(\frac{\partial \zeta_{ik,p}}{\partial x_p} - \frac{\partial \eta_{ik,p}}{\partial x_p}\right) Y^{-}_{kj,p} + (\zeta_{ik,p} - \eta_{ik,p})\frac{\partial Y^{-}_{kj,p}}{\partial x_p}\right\}. \tag{90}$$

Using (16):

$$\frac{\partial \zeta_{ij,p}}{\partial x_p} = \frac{a_i}{\mu_i}\frac{\partial D_p(\mu_i,\mu_j)}{\partial x_p}, \tag{91}$$

$$\frac{\partial \eta_{ij,p}}{\partial x_p} = \frac{a_i}{\mu_i}\frac{\partial D_p(\mu_i,-\mu_j)}{\partial x_p} \tag{92}$$

and from (12) we arrive at the following termination point:

$$\dagger\ \frac{\partial D_p(\mu,\nu)}{\partial x_p} = \frac{1}{2}\sum_{l=m}^{2N-1}\frac{\partial \beta^{*}_{l,p}}{\partial x_p} Y^{m}_{l}(\mu) Y^{m}_{l}(\nu). \tag{93}$$

Note that the derivative in (93) also applies to the derivatives $\partial D_p(\mu,\mu_i)/\partial x_p$ as found in expressions (82) and (88). We must now specify derivatives of the eigenvectors $Y^{-}_{ij,p}$ and eigenvalues $\gamma_{i,p}$ for layer p. We have:

$$\frac{\partial k_{j,p}}{\partial x_p} = \frac{1}{2\sqrt{\gamma_{j,p}}}\frac{\partial \gamma_{j,p}}{\partial x_p}. \tag{94}$$

For the general N-stream case derivatives $\partial\gamma_{j,p}/\partial x_p$ of the eigenvalues and $\partial Y_{j,i,p}/\partial x_p$ for the eigenvectors are determined by explicit differentiation of the eigen-equation together with a constraint provided by the eigenvector normalization. This results in a linear system which can be solved numerically for the required derivatives. The procedure for the general case has been described in [10,11]. The key to this step is to determine first the derivatives of the coefficients of the eigenmatrix $\boldsymbol{\Gamma}$; these follow from the definition (18). We find:

$$\frac{\partial \Gamma_{ij,p}}{\partial \beta^{*}_{l,p}} = \sum_{k=1}^{N}\left\{\left(\frac{\partial \zeta_{ik,p}}{\partial \beta^{*}_{l,p}} + \frac{\partial \eta_{ik,p}}{\partial \beta^{*}_{l,p}}\right)(\zeta_{kj,p} - \zeta_{kj,p}) + (\zeta_{ik,p} + \zeta_{ik,p})\left(\frac{\partial \zeta_{kj,p}}{\partial \beta^{*}_{l,p}} - \frac{\partial \eta_{kj,p}}{\partial \beta^{*}_{l,p}}\right)\right\}. \tag{95}$$

We may use expressions (91)–(93) in the evaluation of the $\boldsymbol{\Gamma}$ derivative. For the 4 and 6 stream cases the differentiation can be performed analytically (see below).

For the particular solutions, derivatives with respect to $\beta^*_{l,p}$ contain no cross-layer terms. We have:

$$\frac{\partial Z_q(\mu)}{\partial x_p} = \frac{1}{2}\sum_{i=-N}^{N}\left\{a_i\frac{\partial D_q(\mu,\mu_i)}{\partial x_q}\delta_{pq}Z_{i,q} + a_i D_q(\mu,\mu_i)\frac{\partial Z_{i,q}}{\partial x_p}\right\}, \tag{96}$$

$$\frac{\partial Z_{i,q}}{\partial x_p} = \frac{1}{2}\left(\frac{\partial W^+_{i,q}}{\partial x_p} + \frac{\partial W^-_{i,q}}{\partial x_p}\right), \quad \frac{\partial Z_{-i,q}}{\partial x_p} = \frac{1}{2}\left(\frac{\partial W^+_{i,q}}{\partial x_p} - \frac{\partial W^-_{i,q}}{\partial x_p}\right). \tag{97}$$

From the auxiliary equation (30) we get:

$$\frac{\partial W^+_{i,q}}{\partial x_p} = -W^+_{i,q}\frac{1}{\lambda_q}\frac{\partial \lambda_q}{\partial x_p} + \frac{1}{\lambda_q}\sum_{j=1}^{N}\left\{\left(\frac{\partial \zeta_{ij,q}}{\partial x_q} - \frac{\partial \eta_{ij,q}}{\partial x_q}\right)\delta_{pq}W^-_{j,q} + (\zeta_{ij,q} - \eta_{ij,q})\frac{\partial W^-_{j,q}}{\partial x_p}\right\}$$
$$+ \frac{1}{\lambda_q\mu_i}\left(\frac{\partial Q^+_{i,q}}{\partial x_q} - \frac{\partial Q^-_{i,q}}{\partial x_q}\right)\delta_{pq}. \tag{98}$$

The derivatives of $Q^{\pm}_i$ follow from (82); the $\boldsymbol{\zeta}$ and $\boldsymbol{\eta}$ derivatives are already noted above in (91) and (92).

The derivatives with respect to λ_q are already given in (85). The other derivatives follow from differentiation of Eq. (19):

$$\frac{\partial d_{i,q}}{\partial x_p} = \frac{1}{\mu_i}(Q^+_{i,q} + Q^-_{i,q})\lambda_q\frac{\partial \lambda_q}{\partial x_p} + \frac{1}{\mu_i}\lambda_p\left(\frac{\partial Q^+_{i,p}}{\partial x_p} + \frac{\partial Q^-_{i,p}}{\partial x_p}\right)$$
$$+ \frac{1}{\mu_i}\sum_{j=1}^{N}\left\{\left(\frac{\partial \zeta_{ij,p}}{\partial x_p} + \frac{\partial \eta_{ij,p}}{\partial x_p}\right)(Q^+_{i,p} - Q^-_{i,p}) + (\zeta_{ij,p} + \eta_{ij,p})\left(\frac{\partial Q^+_{i,p}}{\partial x_p} - \frac{\partial Q^-_{i,p}}{\partial x_p}\right)\right\}. \tag{99}$$

Note that the dependency of λ_q on optical thicknesses is the reason for the existence of non-vanishing cross-layer derivatives of the particular solution. Since λ_q is constant for a plane-parallel medium, the particular solution cross-layer derivatives disappear. In the 4 and 6 stream cases we use the analytic solutions to derive the particular solution derivatives in an explicit analytic form (see below).

4 stream eigensolution derivatives:

$$\frac{\partial \gamma_{i,p}}{\partial x_p} = \frac{1}{2}\frac{\partial \Gamma_{11,p}}{\partial x_p} + \frac{1}{2}\frac{\partial \Gamma_{22,p}}{\partial x_p} \pm \frac{1}{\Xi_p}\left\{\frac{1}{2}(\Gamma_{11,p} - \Gamma_{22,p})\left(\frac{\partial \Gamma_{11,p}}{\partial x_p} - \frac{\partial \Gamma_{22,p}}{\partial x_p}\right)\right.$$
$$\left. + \Gamma_{21,p}\frac{\partial \Gamma_{21,p}}{\partial x_p} + \Gamma_{12,p}\frac{\partial \Gamma_{21,p}}{\partial x_p}\right\}, \tag{100}$$

$$\Xi_p = \sqrt{(\Gamma_{11,p} - \Gamma_{22,p})^2 + 4\Gamma_{21,p}\Gamma_{12,p}}. \tag{101}$$

In (100) the plus sign holds for $i = 1$ and the minus sign for $i = 2$.

$$\frac{\partial Y^-_{11,p}}{\partial x_p} = \frac{\partial Y^-_{22,p}}{\partial x_p} = 0, \tag{102}$$

$$\frac{\partial Y^-_{21,p}}{\partial x_p} = \frac{1}{\gamma_{1,p} - \Gamma_{22,p}} \frac{\partial \Gamma_{21,p}}{\partial x_p} - \frac{\Gamma_{21,p}}{(\gamma_{1,p} - \Gamma_{22,p})^2} \left(\frac{\partial \gamma_{1,p}}{\partial x_p} - \frac{\partial \Gamma_{22,p}}{\partial x_p} \right), \tag{103}$$

$$\frac{\partial Y^-_{12,p}}{\partial x_p} = \frac{1}{\gamma_{2,p} - \Gamma_{11,p}} \frac{\partial \Gamma_{12,p}}{\partial x_p} - \frac{\Gamma_{12,p}}{(\gamma_{2,p} - \Gamma_{11,p})^2} \left(\frac{\partial \gamma_{2,p}}{\partial x_p} - \frac{\partial \Gamma_{11,p}}{\partial x_p} \right). \tag{104}$$

4 stream particular solution derivatives:

$$\frac{\partial W^-_{1,q}}{\partial x_p} = \frac{1}{\Psi_q} \left\{ \Gamma_{12,q} \frac{\partial d_{2,q}}{\partial x_p} + \frac{\partial \Gamma_{12,q}}{\partial x_q} \delta_{pq} d_{2,q} + \left(2\lambda_q \frac{\partial \lambda_q}{\partial x_p} - \frac{\partial \Gamma_{22,q}}{\partial x_q} \delta_{pq} \right) d_{1,q} \right\}$$
$$+ \frac{1}{\Psi_q} \left\{ (\lambda_q^2 - \Gamma_{22,q}) \frac{\partial d_{1,q}}{\partial x_p} - W^-_{1,q} \frac{\partial \Psi_q}{\partial x_p} \right\}, \tag{105}$$

$$\frac{\partial W^-_{2,q}}{\partial x_p} = \frac{1}{\Psi_q} \left\{ \Gamma_{21,q} \frac{\partial d_{1,q}}{\partial x_p} + \frac{\partial \Gamma_{21,q}}{\partial x_q} \delta_{pq} d_{1,q} + \left(2\lambda_q \frac{\partial \lambda_q}{\partial x_p} - \frac{\partial \Gamma_{11,q}}{\partial x_q} \delta_{pq} \right) d_{2,q} \right\}$$
$$+ \frac{1}{\Psi_q} \left\{ (\lambda_q^2 - \Gamma_{11,q}) \frac{\partial d_{2,q}}{\partial x_p} - \frac{W^-_{2,q}}{\Psi_q} \frac{\partial \Psi_q}{\partial x_p} \right\}, \tag{106}$$

$$\frac{\partial \Psi_q}{\partial x_p} = -\left(\frac{\partial \Gamma_{11,p}}{\partial x_p} + \frac{\partial \Gamma_{22,p}}{\partial x_p} \right) \lambda_p^2 + \frac{\partial \Gamma_{11,p}}{\partial x_p} \Gamma_{22,p} + \Gamma_{11,p} \frac{\partial \Gamma_{22,p}}{\partial x_p}$$
$$- \frac{\partial \Gamma_{12,p}}{\partial x_p} \Gamma_{21,p} - \Gamma_{12,p} \frac{\partial \Gamma_{21,p}}{\partial x_p} + [4\lambda_q^3 - 2\lambda_q(\Gamma_{11} + \Gamma_{22})] \frac{\partial \lambda_q}{\partial x_p}. \tag{107}$$

6 stream eigensolution derivatives:

$$\frac{\partial \gamma}{\partial x} = -\frac{\gamma^2(\partial A/\partial x) + \gamma(\partial B/\partial x) + (\partial C/\partial x)}{3\gamma^2 + 2A\gamma + B},$$

$$\frac{1}{Y^-_{1j}} \frac{\partial Y^-_{2j}}{\partial x} - \frac{Y^-_{1j}}{Y^{-2}_{2j}} \frac{\partial Y^-_{1j}}{\partial x} = \frac{\partial}{\partial x} \left\{ \frac{\Gamma_{13}\Gamma_{21} - \Gamma_{23}(\Gamma_{11} - \gamma_j)}{\Gamma_{23}\Gamma_{12} - \Gamma_{13}(\Gamma_{22} - \gamma_j)} \right\},$$

$$\frac{1}{Y^-_{1j}} \frac{\partial Y^-_{3j}}{\partial x} - \frac{Y^-_{1j}}{Y^{-2}_{3j}} \frac{\partial Y^-_{1j}}{\partial x} = \frac{\partial}{\partial x} \left\{ \frac{\Gamma_{12}\Gamma_{31} - \Gamma_{32}(\Gamma_{11} - \gamma_j)}{\Gamma_{13}\Gamma_{32} - \Gamma_{12}(\Gamma_{33} - \gamma_j)} \right\},$$

$$\frac{\partial Y^-_{jj}}{\partial x} = 0 \quad \text{for } j = 1, 2, 3.$$

6 stream particular solution derivatives:

$$\frac{\partial W^-_{k,q}}{\partial x_p} = \frac{\mathrm{Det}(\boldsymbol{M}^{pq}_{(k)})}{\mathrm{Det}(\boldsymbol{M})},$$

$$\{M_{ij}\}^{pq}_{(k)} = \delta_{jk} e^{pq}_i + (1-\delta_{jk}) M_{ij} \quad \text{for } k = 1,2,3,$$

$$e^{pq}_i = \frac{\partial d_{i,q}}{\partial x_p} - \left(2\lambda_q \frac{\partial \lambda_q}{\partial x_p} - \frac{\partial \Gamma_{ij,q}}{\partial x_q} \delta_{pq} \right) W^-_{i,q}.$$

Quantities d_i, M_{ij}, A, B and C were defined and used earlier on pages 8 and 9.

The final task is the evaluation of derivatives of the integration constants $L^{\pm}_{i,q}$ in Eqs. (35) and (38). The way to proceed here is to differentiate the boundary conditions with respect to these optical parameters. Differentiating the layer interface boundary conditions gives:

$$\begin{aligned}
&\sum_{j=1}^{N} \left\{ \frac{\partial L^+_{j,q-1}}{\partial x_p} X^+_{ij,q-1} \Theta_{j,q-1} + \frac{\partial L^-_{j,q-1}}{\partial x_p} X^-_{ij,q-1} - \frac{\partial L^+_{j,q}}{\partial x_p} X^+_{ij,q} - \frac{\partial L^-_{j,q}}{\partial x_p} X^-_{ij,q} \Theta_{j,q} \right\} \\
&\quad = -\sum_{j=1}^{N} \left\{ L^+_{j,q-1} \frac{\partial X^+_{ij,q-1}}{\partial x_{q-1}} \delta_{p,q-1} \Theta_{j,q-1} + L^+_{j,q-1} X^+_{ij,q-1} \frac{\partial \Theta_{j,q-1}}{\partial x_{q-1}} \delta_{p,q-1} \right. \\
&\qquad \left. + L^-_{j,q-1} \frac{\partial X^-_{ij,q-1}}{\partial x_{q-1}} \delta_{p,q-1} - L^+_{j,q} \frac{\partial X^+_{ij,q}}{\partial x_q} \delta_{pq} - L^-_{j,q} \frac{\partial X^-_{ij,q}}{\partial x_q} \delta_{pq} \Theta_{j,q} - L^-_{j,q} X^-_{ij,q} \frac{\partial \Theta_{j,q}}{\partial x_q} \delta_{pq} \right\} \\
&\qquad + \left(\frac{\partial Z_{i,q}}{\partial x_p} - \frac{\partial Z_{i,q-1}}{\partial x_p} \right) F_0 \tilde{T}_{q-1} + (Z_{i,q} - Z_{i,q-1}) F_0 \frac{\partial \tilde{T}_{q-1}}{\partial x_p}
\end{aligned} \tag{108}$$

with $i = -N, \ldots, N$ $(i \neq 0)$ and $q = 2, \ldots, P$ and $p = 1, \ldots, P$. For the boundary condition at TOA, we find similarly that:

$$\begin{aligned}
&\sum_{j=1}^{N} \left\{ \frac{\partial L^+_{j,1}}{\partial x_p} X^+_{ij,1} + \frac{\partial L^-_{j,1}}{\partial x_p} X^-_{ij,1} \Theta_{j,1} \right\} \\
&\quad = -\frac{\partial Z_{i,1}}{\partial x_1} \delta_{1p} F_0 - \sum_{j=1}^{N} \left\{ L^+_{j,1} \frac{\partial X^+_{ij,1}}{\partial x_1} \delta_{1p} + L^-_{j,1} \frac{\partial X^-_{ij,1}}{\partial x_1} \delta_{1p} \Theta_{j,1} + L^-_{j,1} X^-_{ij,1} \frac{\partial \Theta_{j,1}}{\partial x_1} \delta_{1p} \right\}
\end{aligned} \tag{109}$$

with $i = -N, \ldots, 0$ and $p = 1, \ldots, P$. Note that the RHS is zero for $p \neq 1$. Finally, for the boundary condition at the bottom of the atmosphere:

$$\begin{aligned}
&\sum_{j=1}^{N} \left\{ \frac{\partial L^+_{j,P}}{\partial x_p} \hat{X}^+_{ij,P} \Theta_{j,P} + \frac{\partial L^-_{j,P}}{\partial x_p} \hat{X}^-_{ij,P} \right\} \\
&\quad = -\frac{\partial \hat{Z}_{i,P}}{\partial x_p} F_0 \tilde{T}_P - \hat{Z}_{i,P} F_0 \frac{\partial \tilde{T}_P}{\partial x_p} + A \mu_0 F_0 \frac{\partial \tilde{T}_P}{\partial x_p} \\
&\qquad - \sum_{j=1}^{N} \left\{ L^+_{j,P} \frac{\partial \hat{X}^+_{ij,P}}{\partial x_P} \delta_{pP} \Theta_{j,P} + L^+_{j,P} \hat{X}^+_{ij,P} \frac{\partial \Theta_{j,P}}{\partial x_P} \delta_{pP} + L^-_{j,P} \frac{\partial \hat{X}^-_{ij,P}}{\partial x_P} \delta_{pP} \right\}
\end{aligned} \tag{110}$$

which is valid for $i = 0,\ldots,N$ and $p = 1,\ldots,P$. In the last expression we have the auxiliary definitions:

$$\frac{\partial \hat{X}^{\pm}_{ij,P}}{\partial x_P} = \frac{\partial X^{\pm}_{ij,P}}{\partial x_P} - 2A \sum_{k=-N}^{-1} a_k \mu_{-k} \frac{\partial X^{\pm}_{kj,P}}{\partial x_P}, \tag{111}$$

$$\frac{\partial \hat{Z}_{i,P}}{\partial x_p} = \frac{\partial Z_{i,P}}{\partial x_p} - 2A \sum_{k=-N}^{-1} a_k \mu_{-k} \frac{\partial Z_{k,P}}{\partial x_p}. \tag{112}$$

The derivatives of the integration constants with respect to the albedo A in (77) and (81) follow from differentiation of the boundary conditions:

$$\sum_{j=1}^{N} \left\{ \frac{\partial L^{+}_{j,q-1}}{\partial A} X^{+}_{ij,q-1} \Theta_{j,q-1} + \frac{\partial L^{-}_{j,q-1}}{\partial A} X^{-}_{ij,q-1} - \frac{\partial L^{+}_{j,q}}{\partial A} X^{+}_{ij,q} - \frac{\partial L^{-}_{j,q}}{\partial A} X^{-}_{ij,q} \Theta_{j,q} \right\} = 0, \tag{113}$$

$$\sum_{j=1}^{N} \left\{ \frac{\partial L^{+}_{j,1}}{\partial A} X^{+}_{ij,1} + \frac{\partial L^{-}_{j,1}}{\partial A} X^{-}_{ij,1} \Theta_{j,1} \right\} = 0, \tag{114}$$

$$\sum_{j=1}^{N} \left\{ \frac{\partial L^{+}_{j,P}}{\partial A} \hat{X}^{+}_{ij,P} \Theta_{j,P} + \frac{\partial L^{-}_{j,P}}{\partial A} \hat{X}^{-}_{ij,P} \right\}$$

$$\frac{\mu_0 F_0}{\pi} \tilde{T}_P - \frac{\partial \hat{Z}_{i,P}}{\partial A} F_0 \tilde{T}_P - \sum_{j=1}^{N} \left\{ L^{+}_{j,P} \frac{\partial \hat{X}^{+}_{ij,P}}{\partial A} \delta_{pP} \Theta_{j,P} + L^{-}_{j,P} \frac{\partial \hat{X}^{-}_{ij,P}}{\partial A} \delta_{pP} \right\} \tag{115}$$

with

$$\frac{\partial \hat{X}^{\pm}_{ij,P}}{\partial A} = -2 \sum_{k=-N}^{-1} a_k \mu_{-k} \, X^{\pm}_{kj,P} \quad \text{and} \quad \frac{\partial \hat{Z}_{i,P}}{\partial A} = -2 \sum_{k=-N}^{-1} a_k \mu_{-k} Z_{k,P}. \tag{116}$$

3.3. Computational strategy

Differentiation of the boundary conditions produces a linear system for each x_p and for albedo A, from which the derivatives $\partial L^{\pm}_{i,q}/\partial x_p$ and $\partial L^{\pm}_{i,q}/\partial A$ can be determined. These linear systems contain the same (sparse) matrix that was used for the original boundary value calculation; only the source terms differ. The integration constant derivatives are then obtained by back-substitution using the previously determined LU-decomposition of the sparse matrix.

The computational strategy to compute simultaneously the radiance and the weighting functions is the exact reversal of the derivation outlined above. First the optical input parameters and their derivatives with respect to x_p are computed for the specific retrieval application. The first step is to evaluate quantities (and their derivatives) that depend explicitly on the input parameters—these components can be found in equations marked with the † symbol, namely: the three types of transmittances in Eqs. (75), (84) and (79) and the function $D_P(\mu, v)$ in Eq. (93). For the pseudo-spherical model the derivatives of the average secant factors λ_q in Eq. (85) are computed at this stage.

The next step is to calculate eigenvalues, eigenvectors and the particular solution values and their derivatives. Then the sparse matrix and the source terms for the integration constants plus additional source terms for the linear systems that give integration constant derivatives are computed. Back-substitution using the LU-decomposed sparse matrix then provides the constants and their derivatives. Next, the post-processing step is executed by calculating integrated source term components and their derivatives. This requires the eigenvectors and particular solutions plus associated derivatives to be computed at user-defined (off-quadrature) directions μ. The last components that need calculating are those that make up the BOA upwelling radiance and its derivative. Using the layer-by-layer source term integration, we then derive Fourier components of the TOA radiance and TOA radiance derivative for user-defined directions. The Fourier summations then complete the calculations.

The important point to note here is that the LU-decomposition of the sparse boundary problem matrix has to be performed just once for the complete calculation of radiances and weighting functions; this represents an enormous saving in computational effort. Back-substitutions will be done once for the radiance and once for each weighting function. For a multi-parameter retrieval algorithm such as the ozone profile problem for GOME and GOME-2, the simultaneous calculation of weighting functions using a linearized model gives a major advantage in terms of computing time. Furthermore, the weighting functions have been derived analytically by explicit differentiation of the RTE solution; there is no need for ad hoc finite-differencing estimates. A full treatment of boundary condition linearization and weighting function derivation for the general $2N$-stream discrete ordinate model can be found in [10] and [11].

4. Corrections to enhance accuracy

4.1. The delta-M scaling

The delta-M scaling transformation [12] replaces the original phase function by a delta-function forward peak plus a smoother less anisotropic residual. Photons in the forward peak are treated as unscattered; this results in a scaling (reduction) of the optical depth and other optical properties. For single scattering albedo ω_q, optical thickness Δ_q and phase function moment coefficients β_{lq} in layer q, the delta-M scaling is

$$\bar{\omega}_q = \omega_q \frac{(1-f_q)}{(1-g_q)}, \quad \bar{\Delta}_q = \Delta_q(1-g_q), \quad \bar{\beta}_{l,q} = \frac{\beta_{l,q} - (2l+1)f_q}{1-f_q}, \tag{117}$$

where

$$g_q \equiv \omega_q f_q \quad \text{and} \quad f_q = \frac{\beta_{M,q}}{2M+1}. \tag{118}$$

Here, $l = 0, \ldots, 2N-1$ and f_q is the *truncation factor* in layer q, with $M = 2N$. All scaled phase function moment coefficients $\bar{\beta}_{l,q}$ for $l \geqslant M$ are zero. In the pseudo-spherical model, scaling for the slant path optical depth inputs $\tilde{\tau}_p$ follows from the definition (7). In terms of the product $\beta^*_{l,q}$ which governs the discrete ordinate equations, we have:

$$\bar{\beta}^*_{l,q} = \bar{\omega}_q \bar{\beta}_{l,q} = \frac{\beta^*_{l,q} - (2l+1)g_q}{1-g_q}. \tag{119}$$

For the weighting function differentiation with respect to variable x_q in layer q, we also require a scaling of the derivatives $\partial \Delta_q / \partial x_q$ and $\partial \beta^*_{l,q} / \partial x_q$ of the optical input parameters. These may be obtained by straightforward differentiation of the above definitions, and the results are:

$$\frac{\partial \bar{\Delta}_q}{\partial x_q} = \frac{\partial \Delta_q}{\partial x_q}(1-g_q) - \frac{\Delta_q}{2M+1}\frac{\partial \beta^*_{M,q}}{\partial x_q}, \tag{120}$$

$$\frac{\partial \bar{\beta}^*_{l,q}}{\partial x_q} = \frac{1}{(1-g_q)^2}\left\{(1-g_q)\frac{\partial \beta^*_{l,q}}{\partial x_q} - \frac{(2l+1)-\beta^*_{l,q}}{2M+1}\frac{\partial \beta^*_{M,q}}{\partial x_q}\right\}. \tag{121}$$

In the ozone profile application, we do not consider variations of the phase function moments, so that derivatives in (121) are given by $\partial \beta^*_{l,q} / \partial x_q = \beta_{l,q} \partial \omega_q / \partial x_q$. The delta-M scaling is not required for a Rayleigh-only atmosphere, since for $N \geqslant 2$ and $M = 2N$, the Rayleigh phase function moments $\beta^{(\mathrm{Ray})}_{M,q}$ are identically zero.

4.2. Single scatter correction: the Nakajima–Tanaka procedure

The upwelling radiance at TOA calculated by our model may be written in terms of a contribution I_{dms} due to multiple scattering and to the attenuated direct reflection of the solar beam from the surface, and a contribution I_{ss} due to upward single scattering of the solar beam at points along the line of sight. Surface-reflected light (apart from the direct beam) is regarded as multiply scattered; in particular this includes photons scattered singly in *downward* directions before undergoing reflection at the surface. The model computation of I_{ss} is likely to be inaccurate with a low number of streams, since a lot of phase function information is lost in the truncation (with or without the delta-M scaling). A single scatter correction replaces I_{ss} with an exact computation I_{ssexact} which retains an accurate description of the phase function. Using definitions (43) for the TOA intensity mth Fourier component and (44) for the single and multiple scatter layer source terms, we can then perform the Fourier sum over cosine azimuth to get I_{dms} and I_{ss} for a given geometry (μ, ϕ):

$$I_{\mathrm{dms}}(0,\mu,\phi) = \sum_{m=0}^{MC}\left\{\mathscr{B}^m(\mu)T_P(\mu) + \sum_{p=1}^{P} T_{p-1}(\mu)\Lambda^m_{p,(\mathrm{ms})}(\mu)\right\}\cos m(\phi_0 - \phi), \tag{122}$$

$$I_{\rm ss}(0,\mu,\phi) \equiv \sum_{p=1}^{P} T_{p-1}(\mu) S_p^{MC}(\mu,\phi) = \sum_{p=1}^{P} T_{p-1}(\mu) \sum_{m=0}^{MC} \Lambda_{p,({\rm ss})}^{m} \cos m(\phi_0 - \phi). \tag{123}$$

In the last expression the Fourier-summed single scatter layer source term $S_p^{MC}(\mu,\phi)$ has been defined. In calculating the *total* TOA radiance, it is normal practice to apply an accuracy convergence criterion to the Fourier azimuth series for the total (multiple and single scatter) Fourier components. Convergence testing dictates the number MC of terms included in the series; MC is not necessarily equal to $2N-1$ (the maximum allowed number of Fourier terms). However, a single scatter correction means that we need only retain $I_{\rm dms}(0,\mu,\phi)$ from our discrete ordinate model; we do not need expression (123) since this will be replaced by an exact calculation. Thus our model needs to examine convergence only for the multiple scatter radiance, for which the required number of Fourier components may be different from MC which applies to the total radiance. In situations where single scattering tends to predominate (this is true for our application, especially for lower wavelengths in the UV), the multiple scatter Fourier series will in general converge faster than that for the total radiance. This represents a further saving of computer resources. Henceforth in this section, we assume that only multiple scatter output (radiances and weighting functions) has been generated by the discrete ordinate model.

We wish to replace the single scatter contribution $S_p^{MC}(\mu,\phi)$ with quantities $S_p^{\rm exact}(\mu,\phi)$ calculated using a more precise form of the phase function. These corrected single scatter layer source terms may be determined by straightforward integration of the radiative transfer equation in the absence of multiple scatter sources. One can either use the Legendre phase function expansion developed for the discrete ordinate model, taking a sufficient number of phase function moments to ensure an accurate representation of the phase function, or employ an exact expression for the phase function if the latter is available. When the delta-M scaling has been applied, we must implement the single scatter correction using *scaled* optical thickness values, but without scaling the single scatter albedo and by using an exact (unscaled) phase function. In this case a division by $1-g_p$ is necessary because of the scaling on optical thickness (see Eq. (117) above), with $g_p = \beta_{2N,p}^{*}/(2M+1)$ from (118). This calculation is the *first-order NT correction procedure* [13]. For the pseudo-spherical approximation in a non-refracting atmosphere, the total corrected TOA single scatter radiance computed in this way is

$$I_{\rm ssexact}(0,\mu,\phi) \equiv \sum_{p=1}^{P} T_{p-1}(\mu) S_p^{\rm exact} = \sum_{p=1}^{P} T_{p-1}(\mu) \frac{F_0 E_p^0(\mu)}{4\pi(1-g_p)} \sum_{l=0}^{MX} \beta_{l,p}^{*} P_l(\cos\theta_s), \tag{124}$$

where multiplier $E_p^0(\mu)$ is defined in (51).

We have used expansions for the layer phase functions in terms of Legendre polynomials $P_l(\cos\theta_s)$ in the cosine of the scatter angle θ_s, and the number of moments MX is sufficient for an accurate evaluation of the scattering in all layers. θ_s is constant for all layers in a non-refracting atmosphere, and is given by the usual expression:

$$\cos\theta_s = -\mu\mu_0 + \sqrt{(1-\mu^2)(1-\mu_0^2)}\cos(\phi_0 - \phi). \tag{125}$$

In an unscaled atmosphere, $\beta_{2N,p}^{*}$ and hence g_p are zero in each layer, and unscaled optical depths are used in the calculations of $T_{p-1}(\mu)$ and $E_p^0(\mu)$. It is straightforward to write down the derivatives

of (124):

$$\frac{\partial I_{\text{ssexact}}(0,\mu,\phi)}{\partial x_p} = \sum_{q=1}^{P} \left\{ \frac{\partial T_{q-1}(\mu)}{\partial x_p} S_q^{\text{exact}} + T_{q-1}(\mu) \frac{\partial S_q^{\text{exact}}}{\partial x_p} \right\} \tag{126}$$

with:

$$\frac{\partial S_q^{\text{exact}}}{\partial x_p} = \frac{F_0 \delta_{pq} E_q^0(\mu)}{4\pi(1-g_q)^2} \left\{ (1-g_q) \sum_{l=0}^{MX} \frac{\partial \beta_{l,q}^*}{\partial x_q} P_l(\cos\theta_s) + \frac{1}{2M+1} \frac{\partial \beta_{2N,q}^*}{\partial x_q} \sum_{l=0}^{MX} \beta_{l,q}^* P_l(\cos\theta_s) \right\}$$
$$+ \frac{F_0}{4\pi(1-g_q)} \frac{\partial E_q^0(\mu)}{\partial x_p} \sum_{l=0}^{MX} \beta_{l,q}^* P_l(\cos\theta_s). \tag{127}$$

The explicit dependence of (124) on the products $\beta_{l,q}^*$ allows for a straightforward differentiation with respect to these quantities. However, caution should be exercised with the derivatives of the NT-corrected term with respect to quantities such as the asymmetry parameter which impinge upon the phase function moments; the corresponding weighting functions are sensitive to the additional phase function moments which have been included in the exact single scatter calculation but which are absent from the I_{dms} computation. This problem does not arise for derivatives which only affect only the single scattering albedos ω_q; this will be the case in our ozone profile retrieval application. This completes the NT single scatter correction for radiances and weighting functions.

The NT correction has been incorporated in the DISORT code (Version 2.0), where it is automatically applied as a post-processing correction to the radiance output. It has been reported [13,24] that the correction is very effective for all situations away from scattering in the solar aureole region. For this case, Nakajima and Tanaka [13] developed a second-order correction which has also been implemented in DISORT. However, the aureole scenario never pertains in the satellite viewing context, so this refinement will not be necessary in the present application. By way of validation, Table 1 gives some comparisons with DISORT Version 2.0 output, for a 60-layer atmosphere with Rayleigh and aerosol scattering and ozone as the trace gas absorber. Calculations were done at one wavelength (335.4579 nm) for a solar zenith angle of 55°, a relative azimuth of 0° and for a number of line-of-sight viewing angles. The albedo was 0.3. In order to achieve consistency with DISORT, our model was run in plane-parallel mode; all $2N-1$ Fourier terms were included in the results (convergence criterion for the azimuth series was switched off). We compare not only the original uncorrected radiances, but also the single scatter computations I_{ss} and I_{ssexact}.

4.3. Sphericity correction

The treatment in this section is an extension of that given in [11]. As noted in the Introduction, we must consider sphericity effects when dealing with large off-nadir viewing. Referring again to Fig. 1(b), we consider the atmosphere to consist of a number of horizontally homogeneous layers, and we desire the radiance at B. The line-of-sight is now treated in a curved atmosphere, so that the actual solar and line-of-sight path directions will change from A to B. Thus for each layer n, we must define *local* viewing geometries $G_n = \{\alpha_n, \theta_n, \phi_n\}$ for points V_n at the lower layer boundaries ($n = 1,\ldots,P$, where P is the bottom layer of the atmosphere). Here, α_n is the local line-of-sight

Table 1
LIDORT/DISORT comparisons with Nakajima–Tanaka single scatter correction

View angle (degrees)	Stream number	DISORT output	LIDORT output	View angle (degrees)	Stream number	DISORT output	LIDORT output
Original radiance before correction I(original)				*Removed single scatter term I(ss)*			
0.0	6	7.83513E-02	7.835137E-02	0.0	6	2.34218E-02	2.342177E-02
10.0	6	7.64205E-02	7.642062E-02	10.0	6	2.12635E-02	2.126346E-02
20.0	6	7.66746E-02	7.667478E-02	20.0	6	2.05236E-02	2.052363E-02
30.0	6	2.12063E-02	2.120627E-02	30.0	6	7.92090E-02	7.920910E-02
40.0	6	8.41525E-02	8.415261E-02	40.0	6	2.33098E-02	2.330982E-02
Nakajima–Tanaka single scatter term I(ssexact)				*NT-corrected radiance I(corrected)*			
0.0	6	2.36675E-02	2.366747E-02	0.0	6	7.85970E-02	7.859707E-02
10.0	6	2.15248E-02	2.152485E-02	10.0	6	7.66818E-02	7.668200E-02
20.0	6	2.04918E-02	2.049182E-02	20.0	6	7.66428E-02	7.664297E-02
30.0	6	2.08425E-02	2.084254E-02	30.0	6	7.88453E-02	7.884536E-02
40.0	6	2.29805E-02	2.298054E-02	40.0	6	8.38232E-02	8.382333E-02

zenith angle, θ_n the local solar zenith angle (SZA), and ϕ_n the local value of the relative azimuth between two planes containing these directions. The scenario is defined by TOA angles at B, in other words by the geometry G_0 which is the required input. Straightforward ray tracing in a curved atmosphere (with or without refraction) may be used to determine all G_n given the input G_0.

We can again use source-function integration techniques to derive the TOA radiance at B, but this time noting the local dependence on geometry G_n, $n = 1, \ldots, P$. We write for the multiple scatter and direct-beam radiance at B:

$$I^{\mathrm{B}}_{\mathrm{dms}}(0, \alpha_{\mathrm{B}}, \phi_{\mathrm{B}}) = \sum_{m=0}^{MC} \left\{ \mathscr{B}^m(\alpha_A) T^{\mathrm{sph}}_P(\alpha_p) + \sum_{p=1}^{P} T^{\mathrm{sph}}_{p-1}(\alpha_p) \Lambda^{(\mathrm{ms})}_{p,p}(\alpha_p) \right\} \cos m(\phi_0 - \phi_p). \tag{128}$$

The BOA source terms $\mathscr{B}^m(\alpha_A)$ are evaluated for the geometry G_P at A. The line-of-sight transmittance attenuations $T^{\mathrm{sph}}_p(\alpha_p)$ from points V_p to B must now be evaluated for a curved atmosphere. Finally, the multiple scatter *layer* source terms $\Lambda^{(\mathrm{ms})}_{p,p}(\alpha_p)$ for layer p must be computed using geometry G_p. In a similar vein, we have for the single scatter correction:

$$I^{\mathrm{B}}_{\mathrm{ssexact}}(0, \alpha_{\mathrm{B}}, \phi_{\mathrm{B}}) = \sum_{p=1}^{P} T^{\mathrm{sph}}_{p-1}(\alpha_p) S^{(\mathrm{exact})}_{p,p}(\alpha_p, \phi_p), \tag{129}$$

where now the term $S^{(\mathrm{exact})}_{p,p}(\alpha_p, \phi_p)$ for layer p must be evaluated with the appropriate geometry G_p. The final result for radiance I^{B} is obtained by adding the two contributions in (128) and (129); the difference between I^{B} and the regular pseudo-spherical result I_C is the *sphericity correction*.

In particular, we note that solar beam attenuations to points along AB will differ significantly from the attenuations computed for corresponding points along the path AC which is used for the regular pseudo-spherical calculation. Thus it is not surprising that the sphericity correction tends to be dominated by the difference in single scatter computations between paths AB and AC. Computing

transmittances and attenuations for points along AB is straightforward in a curved atmosphere; path distances may be evaluated using the Chapman function or by suitable application of Snell's law in a refractive atmosphere. In a non-refractive atmosphere, the scatter angle is a constant for all points along AB. We now describe an interpolation procedure for speeding up the calculation of I^{B}.

Strictly speaking, we require a series of P calls to the RT model, one for each geometry G_n, $n = 1,\ldots,P$, in order to establish the right multiple scatter layer source terms. However we note that geometries G_n are slowly varying from A to B; an example will illustrate this. We take a non-refractive atmosphere of height 60 km and earth radius 6371 km and TOA input geometry $G_0 = \{65^\circ, 85^\circ, 0^\circ\}$. A simple calculation gives $G_P = \{66.18^\circ, 83.82^\circ, 0^\circ\}$; the change in solar zenith angle is only 1.18°. We expect that the multiple scatter source terms also vary slowly and smoothly with the change in geometry from A to B, and therefore an interpolation procedure using only a few

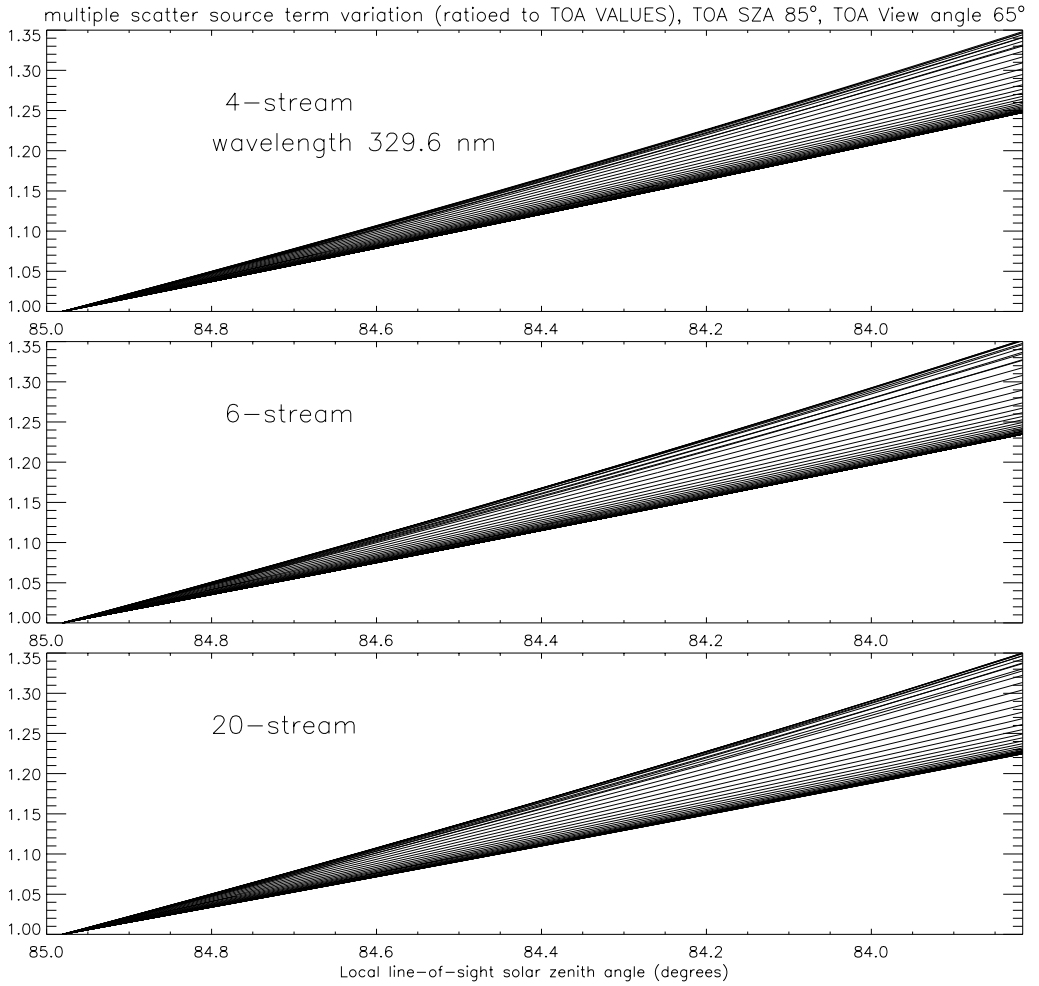

Fig. 2. Dependence of multiple scatter layer source terms with solar angle along line of sight inclined at 65° to the nadir, with corresponding TOA solar zenith angle 85°. Wavelength as indicated, albedo 0.1, reference atmosphere.

Table 2
Maximum interpolation errors (%) for estimating multiple scatter layer source terms

	4 Stream	6 Stream	20 Stream
Linear	0.22410	0.23521	0.24039
Parabolic	2.1056E-03	2.8773E-03	3.3279E-03

RT model calls will be sufficient. For each geometry G_n, there is a complete set $\Lambda^{(\mathrm{ms})}_{n,p}$ of multiple scatter layer source terms, where $p = 1,\ldots,P$. We thus have a matrix of such results, and it is the diagonal entries $\Lambda^{(\mathrm{ms})}_{n,n}$ in this matrix that are required for the sphericity-corrected radiance I^{B}. Fig. 2 plots matrices $\Lambda^{(\mathrm{ms})}_{n,p}$ computed in this manner for a 60-layer mixed Rayleigh/aerosol atmosphere, a TOA geometry $G_0 = \{65^\circ, 85^\circ, 0^\circ\}$, and with optical properties computed at wavelength 329.6 nm. 4 stream, 6 stream and 20 stream LIDORT output is presented. There are 60 lines in total in each graph; the pth line represents source terms $\Lambda^{(\mathrm{ms})}_{n,p}$ for layer p plotted against the geometries G_n as represented by the solar zenith angle variation. Quantities for a given line have been normalized to the values for geometry G_1 (first layer). The dependence is clearly highly linear, suggesting a linear or parabolic interpolation procedure. For the linear interpolation, we choose the end values $\Lambda^{(\mathrm{ms})}_{1,p}$ and $\Lambda^{(\mathrm{ms})}_{P,p}$ ($P = 60$), and for the parabolic case, we select an intermediate point $\Lambda^{(\mathrm{ms})}_{Q,p}$ ($Q = 20$ was chosen). Table 2 shows the maximum interpolation errors obtained using these reference points and interpolating against the solar zenith angle. Linear interpolation (which requires only 2 calls to the RT model) gives errors no greater than 0.25%; the error is negligible for parabolic interpolation (which requires 3 calls to the RT model). Thus the sphericity correction can be implemented satisfactorily with just 1 or 2 additional calls to the RT model; there is no significant loss of accuracy. This is a very important performance consideration for the simulation of backscatter radiances and weighting functions in a retrieval scenario with wide off-nadir viewing geometry.

We note that since the sphericity correction for I^{B} by necessity involves a complete recalculation of the entire single scatter radiation field, it makes sense to use the NT correction right from the outset whenever delta-M scaling has been applied to the discrete ordinate model. In the results that follow, we will adopt this strategy. We use expressions (124) for the radiance and results (126) and (127) for the weighting functions, remembering that different sets of geometries must be used as we sum layer contributions along the line of sight AB.

5. 4/6 stream accuracy: comparisons with 20 stream output

In this section we compare 4 and 6 stream model output with results from LIDORT using 20 streams. Since the low-stream models are intended for use in a fast ozone profile retrieval scheme for a number of nadir viewing space instruments measuring in the UV/visible, we need to look at a wide range of viewing geometries and atmospheric optical properties in the appropriate wavelength range in order to characterize the forward model error. Following a summary description of the scenarios used in this investigation in Section 5.1 below, we then look at the close-to-nadir comparisons without the sphericity correction (Section 5.2), before moving on to the wide-angle viewing scenarios in Section 5.3.

5.1. Atmospheric setup and viewing scenarios

All calculations were performed on a 60-level grid from 0 to 60 km, with vertical resolution of 1 km throughout. Temperature, pressure and ozone volume mixing ratio profiles for the Tropical AFGL standard atmosphere were used [25]. Temperature-dependent cross sections for the ozone Hartley and Huggins absorption bands were taken from a standard data set [22]. Rayleigh scattering properties were determined using empirical formulae for the scattering coefficient and depolarization ratio [26] taken from the data of Bates [27]. A background aerosol distribution was taken from the MODTRAN database [28], with a maritime regime in the planetary boundary layer (visibility 25 km), and background loading and optical properties in the troposphere, stratosphere and mesosphere. Aerosol phase functions were approximated by the Henyey–Greenstein form, with asymmetry parameters also taken from the MODTRAN data set. The lower boundary of the atmosphere was treated as a Lambertian surface; four albedo values were chosen in this study (0.05, 0.1, 0.3 and 0.7).

This constitutes our clear-sky reference atmosphere. For cloud scenarios, we took a cloud layer of geometrical thickness 1.0 km between 3.0 and 4.0 km and varied the optical thickness (7 values of τ_{cloud} were chosen; 0.25, 0.50, 1.0, 2.0, 5.0, 10.0 and 20.0). The cloud particulate (water droplet) single scattering albedo was taken to be 0.999, with corresponding asymmetry parameter 0.85.

For the special cases involving optically thick particulate layers, we selected the following: (1) a Saharan dust scenario, consisting of a layer of dust 1 km thick between 6 and 7 km, with optical thickness 1.0, single scattering albedo 0.83 and asymmetry parameter 0.79, the latter two values taken from the MODTRAN dust model; (2) a volcanic ash scenario, with a layer of ash at 16–17 km, with extinction and scattering coefficients 0.05641 (km^{-1}) and 0.4494 (km^{-1}) respectively, and asymmetry parameter 0.7897; and (3) a polluted planetary boundary layer scenario, with a layer of particulates at 0–1 km with extinction coefficient 2.9462 (km^{-1}), scattering coefficient 1.893 (km^{-1}) and asymmetry parameter 0.7067. Optical properties for cases (2) and (3) were taken from the LOWTRAN aerosol data base, namely a "fresh volcanic" aerosol loading for case (2) and an "urban" planetary boundary layer aerosol with visibility 2 km for case (3). Optical properties were taken be constant with wavelength (the values at 337.1 nm were used). All phase functions were treated using the Henyey–Greenstein form.

Calculations were performed for a wavelength range of 299–335 nm. Below 300 nm, multiple scattering effects are minor and the issue of RT model errors correspondingly less important owing to the strong ozone absorption and increasing predominance of the Rayleigh single scattering contribution. [Single scatter computations are entirely sufficient for RT simulations below 295 nm.] For the full-wavelength runs, a spectral resolution of $\sim$0.5 nm was adopted. For detailed studies, we selected six wavelengths spread over the Hartley–Huggins bands, from 309.5 to 335.5 nm at $\sim$5.5 nm spacing. The range of solar zenith angles θ_0 used was 15–85°. For the relative azimuth angle $\phi_0 - \phi$ at TOA between the solar plane and the line-of-sight plane, we used the two values 0° (solar) and 180° (antisolar). For detailed studies using the close-to-nadir pseudo-spherical models without the sphericity correction, we chose values of the line-of-sight zenith angle from 0° to 40°. For investigations with the sphericity correction, some 34 values of the line-of-sight zenith angles were taken from $-70°$ on the antisolar side to $+70°$ on the solar side. This range is wide enough to include the extreme OMI and GOME-2 swath positions.

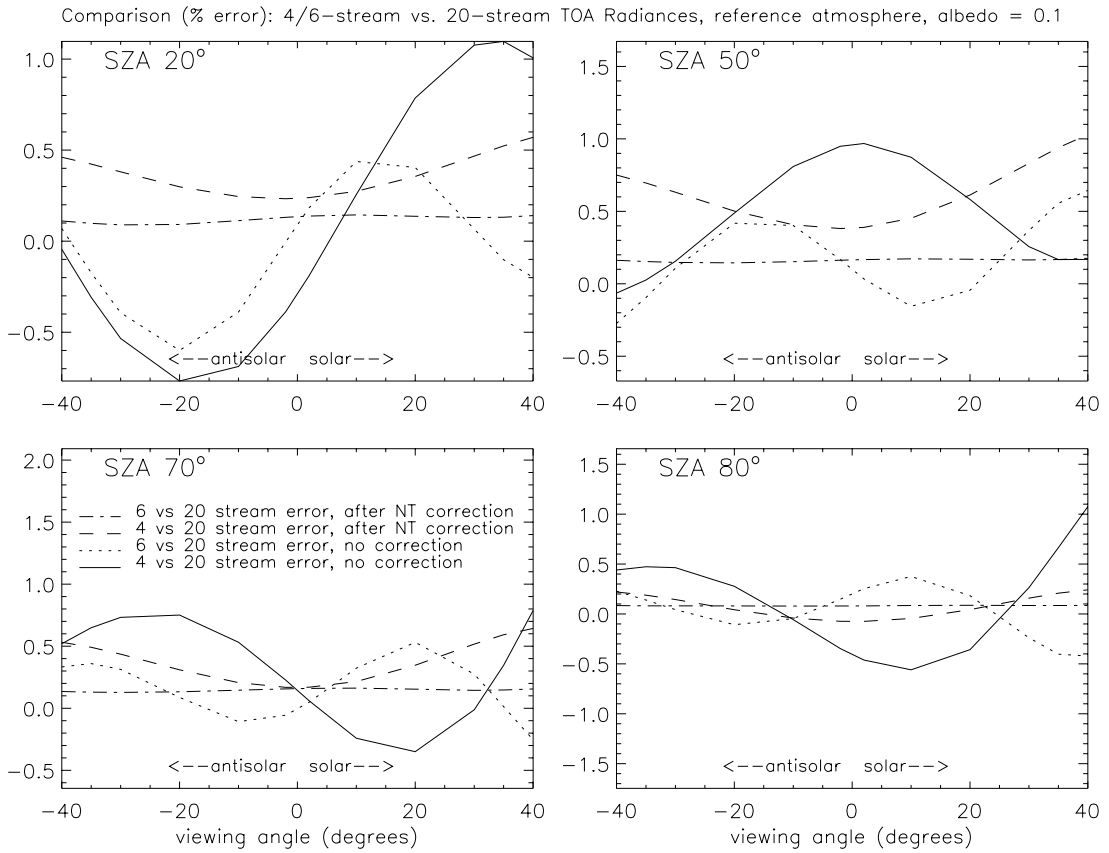

Fig. 3. Comparison of 4/6 stream and 20 stream TOA upwelling radiances for a reference atmosphere with background aerosol loading; wavelength 329.002 nm, solar zenith angles as indicated.

5.2. Close-to-nadir viewing: the Nakajima–Tanaka correction

We first look at the effect of the NT single scatter correction at one wavelength (329.0015 nm). Working with the clear sky reference atmosphere, we take an albedo of 0.1 and four solar zenith angles (20°, 50°, 70° and 80°), with a range of line-of-sight zenith angles from −40° on the antisolar side to +40° on the solar side. Fig. 3 shows comparisons between 4 stream and 6 stream TOA radiance output against 20 stream LIDORT results, with and without the NT correction. Wave structures in the uncorrected output reflect preferential scattering which is not well accounted for by the uncorrected RT model. For the 4 stream case, these structures are damped upon application of the NT correction, and the overall error level is reduced by a factor of 2. However, there are still situations for which the 4/20 radiance difference has increased even after the correction. The situation is much improved with the 6 stream case; the wave structures have almost entirely disappeared and the error has been reduced to a constant low value of around 0.2–0.25%. Thus it is clear that there is a substantial improvement between 4 and 6 streams.

The situation for a sample of ozone volume mixing ratio weighting function profiles is shown in Fig. 4. The scenario is the same as that used for Fig. 3, except that we consider only one

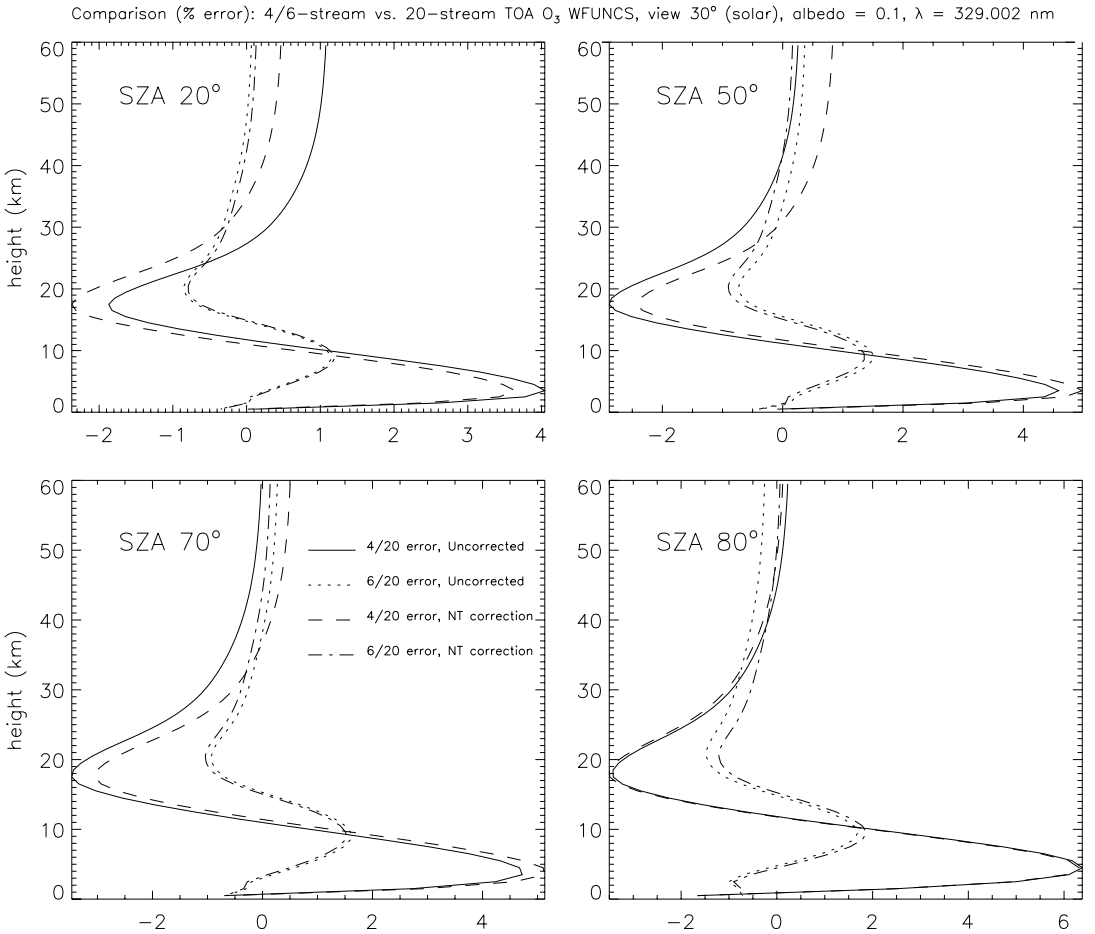

Fig. 4. Comparison of 4/6 stream and 20 stream TOA upwelling ozone volume mixing ratio weighting functions for a reference atmosphere with background aerosol loading; wavelength 329.002 nm, solar zenith angles as indicated. Line of sight angle 30° on the solar side.

line-of-sight zenith angle (30° on the solar side). The first thing to notice is that the NT correction has little effect on the weighting function accuracy; this should not surprise us, since the weighting functions represent relative changes in the radiance with respect to changes in ozone distributions. A factor of 3 improvement in the error is apparent with the 6 stream case over the 4 stream values; 6 stream weighting functions are nowhere more than 2% distant from their 20 stream equivalents. Peak sensitivity for these weighting functions is around 25 km (this is a tropical atmosphere), and the absolute values of these weighting functions below the tropopause (~17.5 km) are small. Thus the major uncertainty in the weighting function profile occurring in the troposphere should not concern us unduly, as there is little information to be gained in the retrieval from this part of the atmosphere.

It is well known that Rayleigh scattering is dominant in this part of the UV, especially for shorter wavelengths. We would therefore expect in general that the effects of aerosol scattering will be small on the radiance differences, with the largest discrepancies occurring at higher wavelengths

where aerosol scatter is more pronounced. Below 300 nm the magnitude of backscatter is controlled almost entirely by Rayleigh single scattering, and there is little contribution from surface reflected light and tropospheric scattered light because of strong ozone absorption in the Hartley bands (the total ozone absorption optical depth at 290 nm is typically $\simeq 12$). For a Lambertian surface, the reflected (unscattered) direct solar beam is increasingly important for higher surface albedos, and we would expect 4/20 and 6/20 radiance differences to become smaller for high albedos.

We now consider more extensive comparisons for a wavelength range of 299–335 nm, and for 26 solar zenith angles from 15° to 85°. Fig. 5 is a contour plot that shows both the 4 and 6 stream comparisons with and without the NT correction, for the reference atmosphere with an albedo of 0.05 and a viewing zenith angle of 20° in the solar direction. The most prominent feature in the uncorrected 4/20 comparison (upper panel) is the broad maximum centered around solar zenith angle 35° and extending from 315 nm upwards. This is the preferential direction for combined molecular and aerosol single scattering in the atmosphere. Wave structures are apparent in both the uncorrected results, with the wave amplitude following the change in solar zenith angle. The preferential maximum and the wave structures are greatly reduced in the corrected 4 stream results, and almost totally absent for the 6 stream comparisons. We also observe that differences show some variation with the differential structure of the Huggins bands ozone absorption, particularly for high solar zenith angles. It is clear that differences are small for the shorter Rayleigh-dominated wavelengths.

We present detailed contour plots for two more scenarios. Fig. 6 shows some 6 stream comparisons for an atmosphere with a cloud layer at 3–4 km, which has optical properties as noted above in Section 5.1. The scenario is for an off-nadir view of 20°, an albedo of 0.1 and a relative azimuth of 0°. Results for three cloud optical thickness values are shown. It is clear that once the optical depth reaches a certain value, the albedo effect kicks in and the cloud behaves increasingly like a reflecting surface—the 6 stream accuracy becomes greater the thicker the cloud (the same behavior was also found in the corresponding 4 stream comparisons). The optical depth value giving the highest level of error in this case is 2.0, with the maximum uncorrected error in excess of 2.0% for wavelengths greater than 325 nm and for solar zenith angles in the range 15–30° (center left panel). The wave structure is clear in the left-hand (uncorrected) panels. We note that for cloud layers closer to the surface, the effect will increasingly resemble that produced by a highly reflecting surface, so we would expect the 6/20 differences to be smaller in this case. By contrast, a particulate layer higher in the troposphere would be expected to produce more significant errors, and we observe this to be the case in the next scenario (Saharan dust).

In the ozone profile algorithms developed so far for GOME, SCIAMACHY and GOME-2, clouds have been treated in the independent pixel approximation, wherein the simulated TOA radiance for a partially cloudy scene is taken to be a weighted mean of two radiances for clear-sky and cloud-filled scenarios:

$$I_{\text{total}} = F_{\text{c}} I_{\text{cloud}} + (1 - F_{\text{c}}) I_{\text{clear}}. \tag{130}$$

F_{c} is the fractional cloud cover. For GOME scenes, F_{c} has been retrieved either by using reflectivity measurements in and around the O_2 A band [29–31], or by means of a thresholding algorithm based on GOMEs broad-band polarization measurement devices [31]. O_2 A band reflectivities can also yield information on cloud-top pressure values and cloud optical thickness, though it has not yet proved possible to obtain consistently reliable estimates of the latter quantity. In the FRESCO

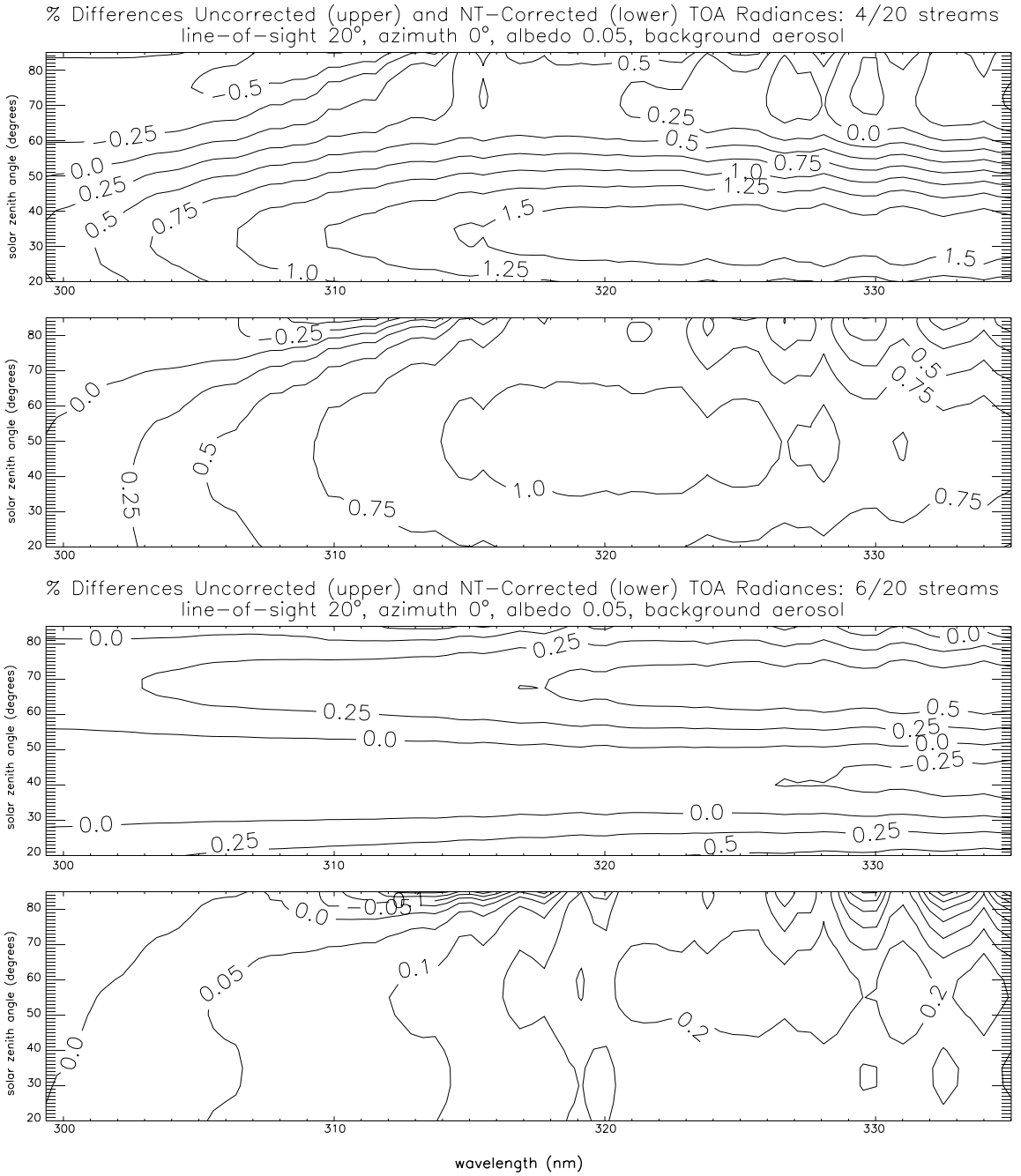

Fig. 5. Comparison of 4/6 stream and 20 stream TOA upwelling radiances for a reference atmosphere with background aerosol loading; wavelength range 299–335 nm, solar zenith range 15–85°.

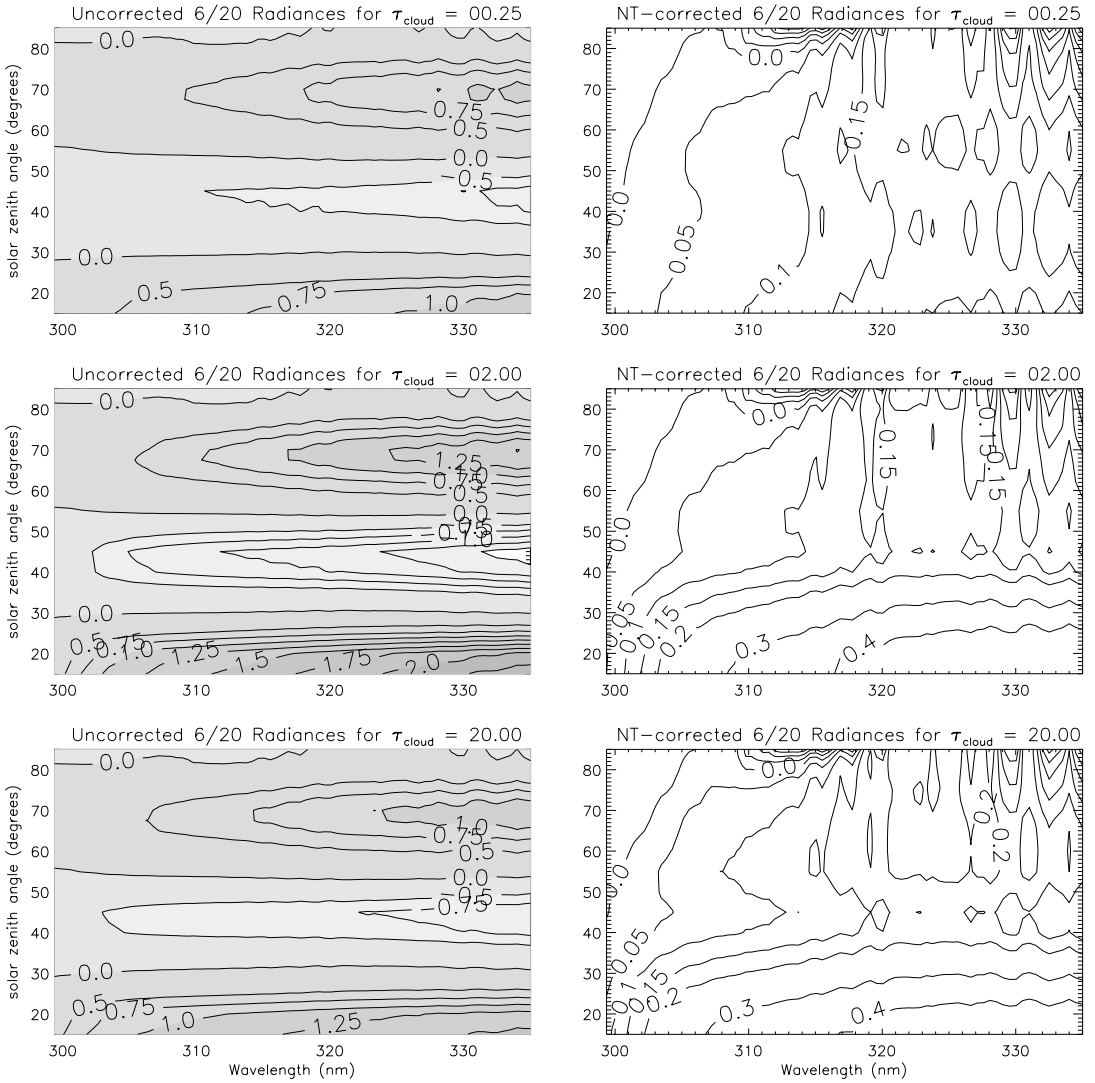

Fig. 6. Differences (expressed as percentages) between 6 stream and 20 stream TOA upwelling radiances for a reference atmosphere with cloud layer between 3–4 km with 3 cloud optical thickness values as indicated. Viewing zenith 20°, azimuth 0°, albedo 0.1. Wavelength and solar zenith ranges as in Fig. 5.

algorithm [30], clouds are treated as Lambertian reflectors with albedo 80%, and least-squares fitting of reflectivities in part of the O_2 A band yields a simultaneous retrieval of cloud fraction F_c and cloud-top pressure p_c. With the large GOME footprint, F_c and p_c must be regarded as *effective* values which in the context of ozone profile or column retrieval are used to correct for the trace gas distribution in the lower part of the atmosphere. These results from FRESCO are used in the Fast Delivery ozone processor at KNMI.

The previous example showed that the presence of an additional scatterer in one part of the atmosphere can introduce larger differences between 4/6 stream and 20 stream radiances, particularly

if the layer has a critical optical depth. If the scatterer is optically thin in the chosen layer, then there will not be much difference from background results. On the other hand a really opaque particulate layer will act as a reflecting boundary with high albedo, in which case the change from 4/6 to 20 streams will be reduced for reasons given above. For the three special cases described in Section 5.1, we look at the same viewing conditions as in the cloud examples. In Fig. 7 (top panels) results are shown for the Saharan dust layer scenario; the major positive error peak in the uncorrected results around solar zenith angle 70° has increased to 2.2% by comparison with the cloud case (the corresponding number for the 4 stream comparison was greater than 3.5%). By contrast, the NT-corrected results (upper right) show little structure, with error levels below 0.5%. (Contour levels are at intervals of 0.5% for the uncorrected results, and generally at 0.1% for the NT-corrected comparisons). For the volcanic ash layer scenario, we would not expect 4/20 and 6/20 differences to be greatly in excess of those generated using the reference atmosphere. This remark follows from the consideration of optical depth; although the extinction coefficient for the volcanic layer is two orders of magnitude above background levels, the layer is still optically thin compared to the Saharan dust model. These remarks are borne out by the 6/20 stream comparisons in Fig. 7 (middle panels).

For the planetary boundary layer scenario with an optically thick aerosol layer near the surface, we would expect this situation to resemble a reasonably highly reflecting surface. In Fig. 7 (lower panels) the comparisons are done for 4 streams. The general error level is not greatly different from the clear sky case. The interesting thing to note here is that in contrast with the other two 6/20 stream comparisons in Fig. 7, the NT-corrected 4/20 stream results in the lower right panel are actually worse than the uncorrected ones for sizeable ranges of wavelength and solar zenith angle. Geometry-dependent structures are present in both the lower panels, though the preferred direction has changed from uncorrected to NT-corrected. This example demonstrates clearly that 4 stream models should be used with caution; it is safer and more accurate with 6 streams.

Although the dust scenario is admittedly an extreme situation, it does help to establish accuracy limits for the low-stream models. This scenario has special significance in the ozone profile retrieval context. An algorithm to indicate the presence of absorbing aerosols in the lower atmosphere was first developed for the total ozone monitoring spectrometer (TOMS) instrument in order to look at anomalous ozone column results obtained in biomass burning (smoke aerosols) and dust-outbreak scenarios [32–34]. The algorithm examines the radiances at two different wavelengths and computes the spectral residue upon subtraction of the Rayleigh contribution to the backscatter. It turns out that this residue (the aerosol absorbing index) is a clear indicator for the presence of absorbing aerosols. The algorithm has now been applied to GOME measurements [35], and will also be used operationally for GOME-2 and SCIAMACHY. The point here is that if there is a clear indication of the presence of an absorbing aerosol layer in a given GOME or GOME-2 footprint, then we can use this information to switch from a 4 stream model to a 6 stream calculation of backscatter radiances and weighting functions required for an ozone (profile or column) retrieval.

Results for the reference and cloud-layer scenarios are summed up in Table 3, along with the above-mentioned three special cases. The table gives an overview of the maximum and minimum differences to the 20 stream output, both for uncorrected and NT-corrected TOA radiance values. The first four reference scenarios (Ref 1 to Ref 4) are intended to examine the albedo dependence; as noted above the errors increase with decreasing albedo. The Ref 2 and Ref 5–7 scenarios together give an indication of the off-nadir viewing angle dependence; for the uncorrected results, both 4

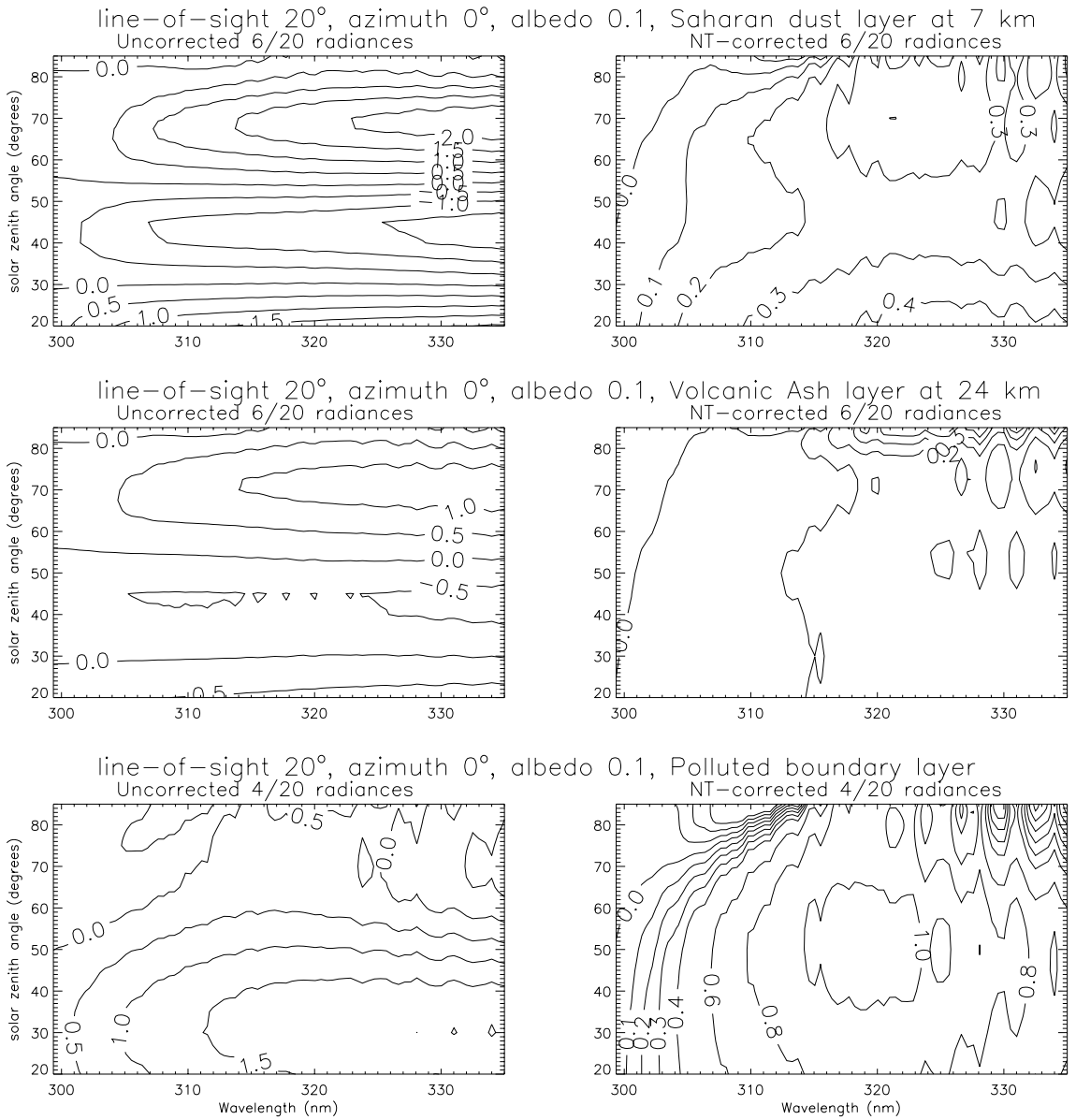

Fig. 7. Comparison of TOA upwelling radiances for three special cases: (top panels) 6/20 differences with layer of desert dust at 6–7 km; (center panels) 6/20 differences with volcanic ash layer at 24 km; (lower panels) 4/20 differences with polluted boundary layer. Viewing zenith 20°, azimuth 0°, albedo 0.1. Wavelength and solar zenith ranges as in Fig. 5.

stream and 6 stream errors increase as the viewing angle moves away from the nadir, but this dependence is absent for the NT-corrected equivalents. Cloud-layer scenarios show the cloud optical thickness dependence; all results show a clear peak in the maximum error values for optical thickness $\tau_{\text{cloud}}=2.0$. Finally, we note that the Saharan dust scenario has the largest 6 stream error. In summary,

Table 3
Maximum and minimum % errors for uncorrected and NT-corrected TOA radiance output

Scen	Alb. τ_{cloud}	View	Azm	Uncorrected				NT-corrected			
				4 Stream		6 Stream		4 Stream		6 Stream	
				Max	Min	Max	Min	Max	Min	Max	Min
Ref 1	0.05	20.0	0.0	1.721	−0.757	0.720	−0.362	1.139	−0.612	0.248	−0.217
Ref 2	0.10	20.0	0.0	1.596	−0.763	0.684	−0.337	1.069	−0.619	0.241	−0.216
Ref 3	0.30	20.0	0.0	1.208	−0.794	0.608	−0.303	0.834	−0.651	0.220	−0.214
Ref 4	0.70	20.0	0.0	0.732	−0.900	0.481	−0.287	0.565	−0.726	0.217	−0.207
Ref 5	0.10	2.0	0.0	1.416	−1.030	0.610	−0.224	0.860	−0.661	0.249	−0.234
Ref 6	0.10	10.0	0.0	1.504	−1.041	0.656	−0.267	0.891	−0.656	0.253	−0.230
Ref 7	0.10	30.0	0.0	1.622	−0.420	0.791	−0.735	1.300	−0.555	0.231	−0.200
Cld 1	00.25	20.0	0.0	2.120	−0.949	1.174	−0.867	1.074	−0.625	0.225	−0.212
Cld 2	00.50	20.0	0.0	2.554	−1.288	1.561	−1.226	1.050	−0.630	0.274	−0.208
Cld 3	01.00	20.0	0.0	3.077	−1.685	2.055	−1.564	1.010	−0.641	0.393	−0.203
Cld 4	02.00	20.0	0.0	3.415	−1.961	2.407	−1.659	1.041	−0.741	0.556	−0.196
Cld 5	05.00	20.0	0.0	3.054	−2.112	2.246	−1.404	1.176	−0.928	0.630	−0.189
Cld 6	10.00	20.0	0.0	2.476	−1.954	1.867	−1.151	1.011	−0.989	0.576	−0.189
Cld 7	20.00	20.0	0.0	2.051	−1.779	1.572	−0.986	0.757	−1.012	0.493	−0.190
Sahar	0.10	20.0	0.0	2.675	−4.172	2.439	−1.895	0.406	−1.778	0.452	−0.164
Volcn	0.10	20.0	0.0	2.049	−1.366	1.283	−0.641	1.721	−0.550	0.557	−0.086
Polld	0.10	20.0	0.0	2.025	−0.738	1.023	−0.476	1.091	−0.593	0.294	−0.216

we note that in all cases, the NT-corrected 6 stream results are within 0.65% of their 20 stream equivalents, and that in clear sky circumstances, these errors are mainly at the 0.25% level or below. For the corrected 4 stream results, the reference clear sky errors are in the 1.0–1.3% range and cloud-layer errors are roughly the same; however two of the special cases are still showing absolute errors at the 1.75% level.

5.3. *Wide-angle viewing: the sphericity correction*

We wish to compare sphericity-corrected output for the path AB with regular pseudo-spherical RT calculations for a scattering path AC based on the geometry at point A. We will be comparing two sets of NT-corrected data in order to isolate the sphericity effect. This time we take line-of-sight viewing angles from -70° in the antisolar direction to $+70^\circ$ in the solar direction. Fig. 8 shows results for the TOA radiance for the reference atmosphere with albedo 0.1, for a selection of 6 wavelengths and 4 solar zenith angles. Three separate RT model runs were done for the multiple scatter terms along AB, with parabolic interpolation used to determine intermediate values as described in Section 4.3. Note that the correction has the same sign for lower values of the solar zenith angle, but reverses for high solar zenith angles. This is a function of the sun's position in front or behind the line of sight. The correction is also much larger for high solar zenith angles, where attenuation along the direct solar beam is critical.

The magnitude of the sphericity correction is very much the same for 4, 6 and 20 stream calculations. This should not surprise us, since as already noted, its magnitude is strongly dependent on the

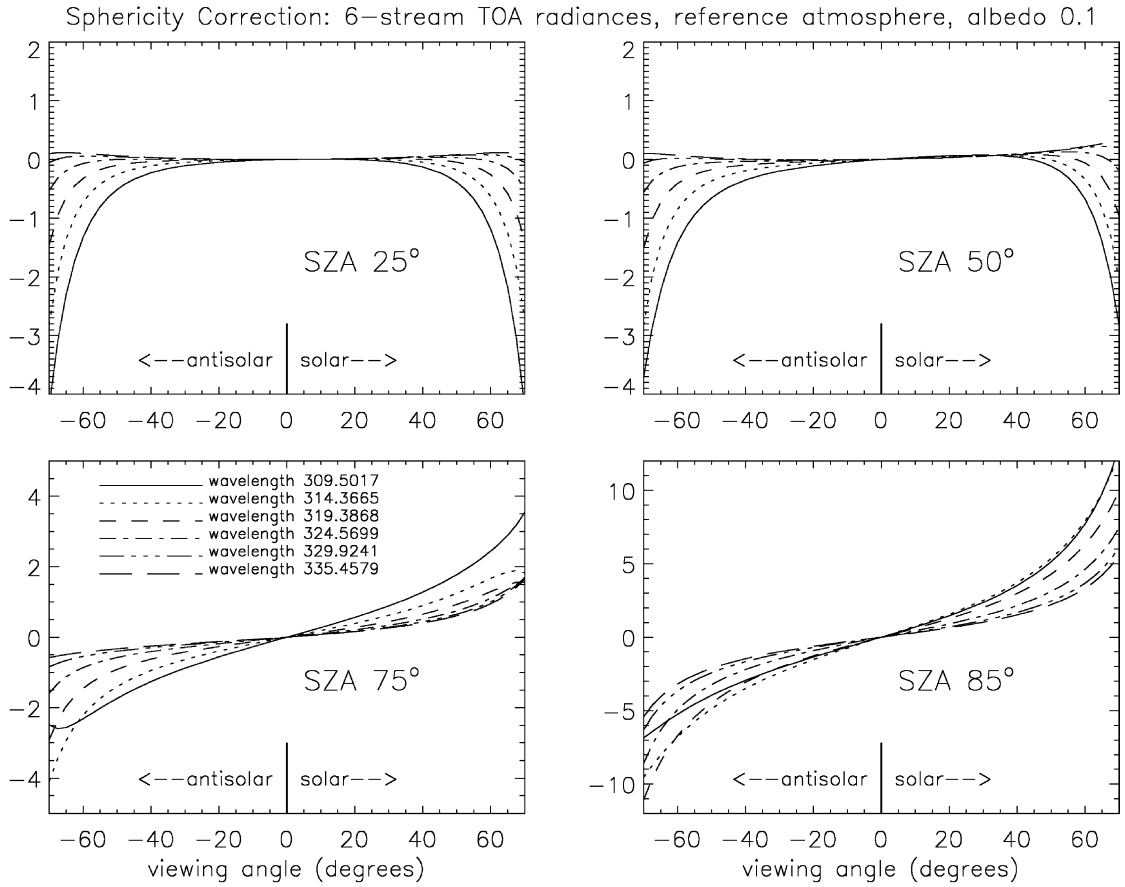

Fig. 8. Sphericity correction 6 stream TOA upwelling radiances for a reference atmosphere with albedo 0.1. Viewing zenith angle range -20° to $+40^{\circ}$. Wavelength and solar zenith ranges as indicated.

single scatter calculations to point along the path AB. It is immediately obvious that this correction is important for the wide angle view. Indeed for a solar zenith angle of 85°, the line-of-sight zenith angles are restricted to the range $[\pm 15.9^{\circ}]$ at 319.4 nm if the sphericity correction is to be ignored at the 1% level. Even for a solar zenith angle of 50°, viewing paths outside the range $[+62.7^{\circ}, -55.7^{\circ}]$ will be outside the 1% threshold for the sphericity correction. Another way of looking at these results is to plot thresholds for the absolute sphericity correction. In Fig. 9, this is done for thresholds from 0.5% to 8.0% (contours as marked) and for a wide wavelength range. The GOME ($\sim 34.6^{\circ}$) and GOME-2 ($\sim 55.7^{\circ}$) swath limits are marked; the OMI swath limit is at $\sim 67.4^{\circ}$. Clearly the sphericity effect for GOME can be ignored to the 1% level for solar zenith angles up to 75°, but it becomes significant at the 2% level at sun angle 85°. For GOME-2, the sphericity correction is needed to the 2% level at SZA 75°, and at the 5% level at 85°. The situation with OMI is even more serious. Notice also the asymmetry between solar and antisolar directions, and at SZA 75° the change in sign of the correction for wavelengths near 300 nm. The increasingly high ozone absorption in this part of the UV can have a critical effect on the attenuation along both the solar beam

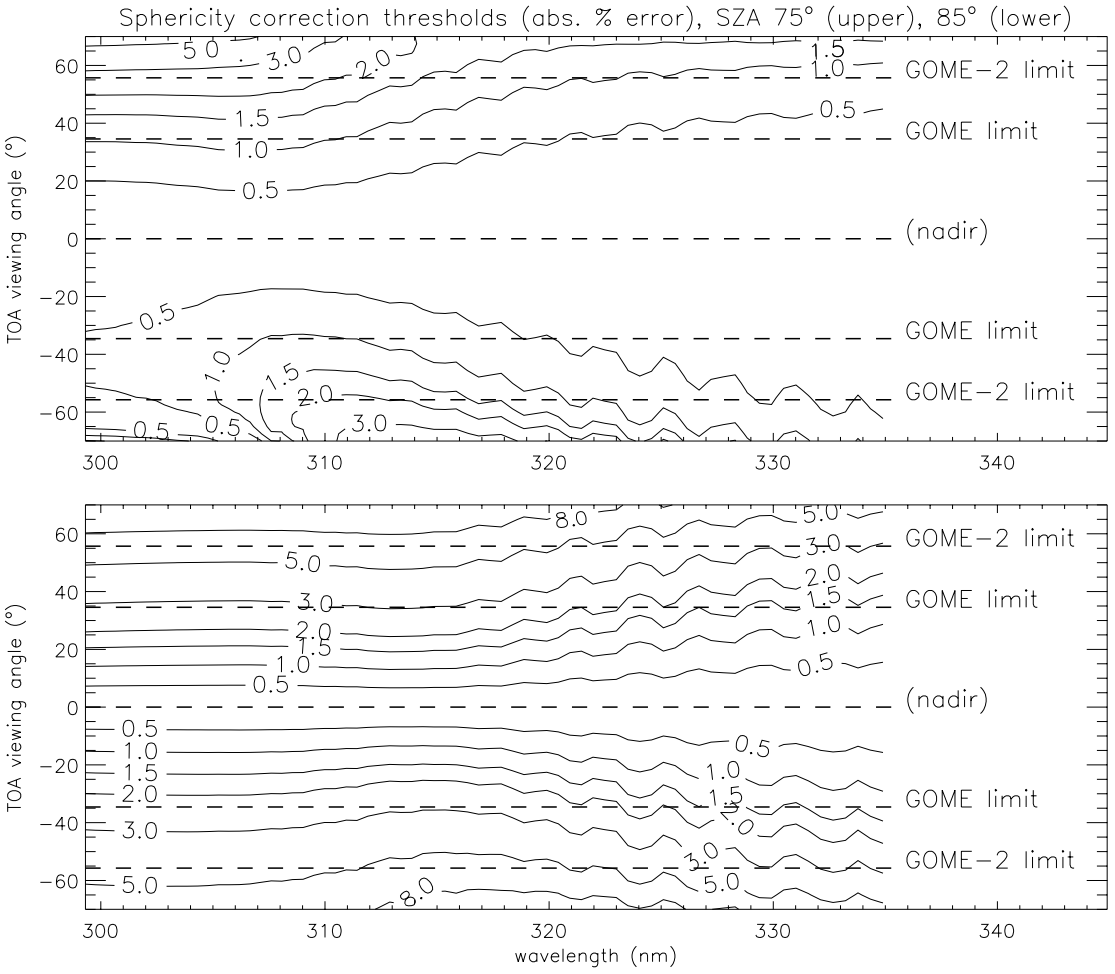

Fig. 9. Sphericity correction thresholds for 6 stream TOA upwelling radiances for a reference atmosphere with albedo 0.1, and for 2 solar zenith angles. Wavelength against line-of-sight viewing angle.

and the line-of-sight path. Given this sort of variability, it is not an easy matter to decide when to implement the sphericity correction, and this will have consequences for the retrieval algorithm.

A similar picture pertains for the weighting functions. Since the sphericity effect is much the same no matter what the scattering accuracy, we focus on 6 stream output only, looking at weighting function profiles with respect to ozone volume mixing ratio in our reference atmosphere, again assuming an albedo of 0.1. Fig. 10 shows results for 4 solar zenith angles at a wavelength of 329.5 nm, and for line-of-sight viewing angles corresponding to the GOME, GOME-2 and OMI swath limits. From the graphs, we see that for solar zenith angles up to 75°, the sphericity correction can be ignored for GOME at the 1% level, and for GOME-2 at the 2% level. At SZA 85°, weighting function errors due to the neglect of the sphericity correction are up to 2% for GOME and as high as 5% for GOME-2. The situation for OMI is more serious, with significant errors at all solar zenith angles, ranging from a +5% maximum at SZA 20°, to −12% at SZA 85°. In common with the

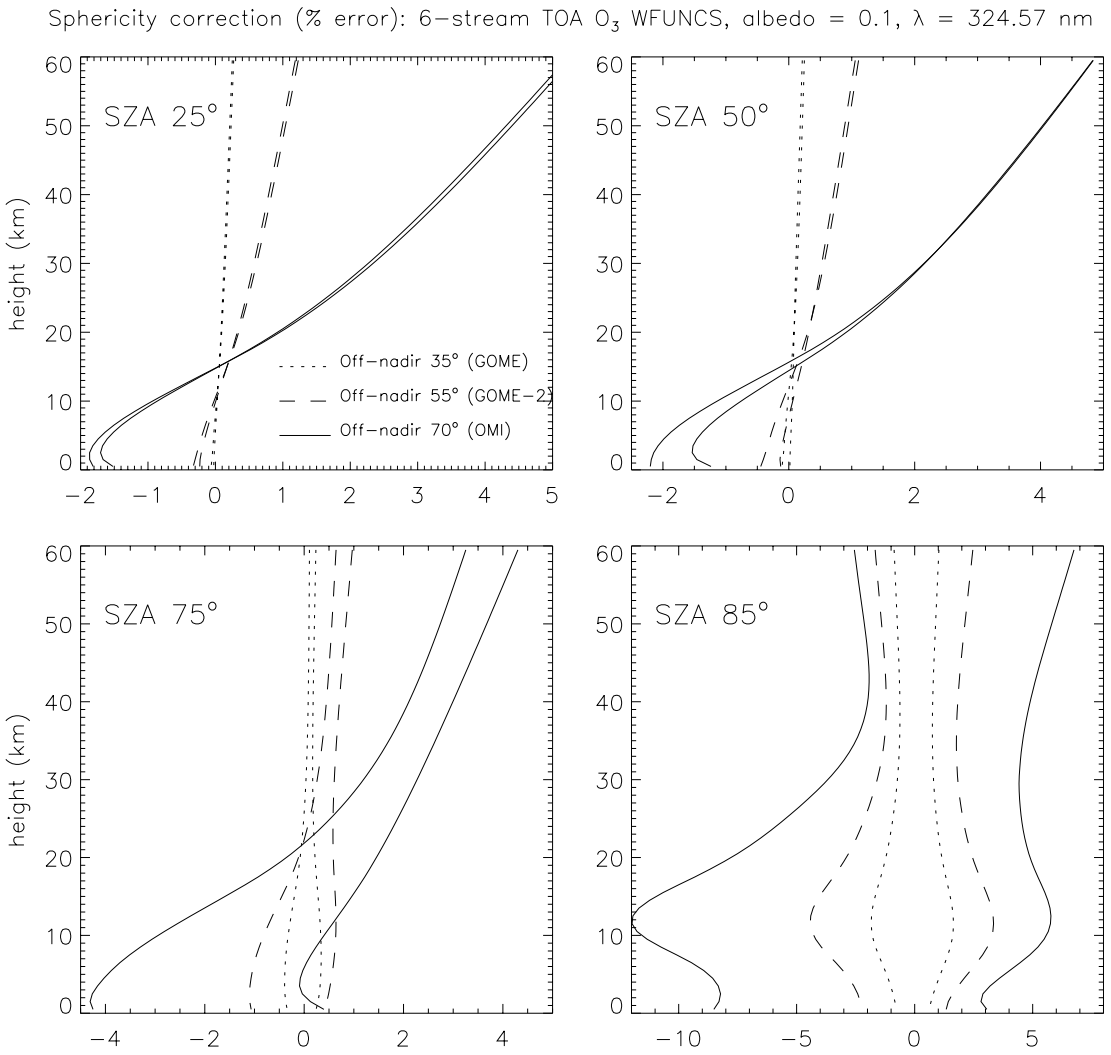

Fig. 10. Sphericity correction for 6 stream TOA upwelling ozone volume mixing ratio weighting functions, for a reference atmosphere with albedo 0.1, for wavelength 324.57 nm. Solar zenith angles as in Fig. 8.

results in Fig. 8, the sphericity correction has the same sign for lower SZA values, but has the opposite sign for all off-nadir angles at SZA 85°.

6. Discussion: relevance to ozone profile retrieval

In this paper, we have determined analytic 4 and 6 stream solutions for radiances and weighting functions using a linearized discrete ordinate model. In order to determine the model's suitability for use in a fast and accurate ozone profile retrieval algorithm using UV backscatter measurements from nadir viewing instruments such as GOME, GOME-2, SCIAMACHY and OMI, we have carried

out a detailed investigation of the model accuracy for a range of atmospheric scenarios appropriate to this retrieval application. Comparisons for radiance and a limited number of weighting functions were carried out against the general model LIDORT operating in the 20 stream discrete ordinate approximation. We have shown that significant improvments to the accuracy can be gained by using a post-processing correction for the single scatter contribution to the upwelling radiance. Further, it was shown that a sphericity correction is an essential requirement for wide-angle off-nadir viewing, particularly for high solar zenith angles.

We show that with a few exceptions, the NT-corrected 4 stream model is accurate to 1.25% for the vast majority of clear sky scenarios likely to be encountered in the retrieval of ozone profiles from backscatter UV spectrometers in space. The major exceptions occur in the presence of additional moderately thick particulate layers at high levels in the troposphere. The template for this is the Saharan dust model. It is noted that this situation can be flagged in an operational environment provided that the presence of such a layer can be established by means of a suitable absorbing aerosol indexing algorithm. The single scatter corrected 6 stream model is shown to reproduce 20 stream radiance values $> 0.65\%$ for all scenarios considered, with corresponding weighting function accuracy to $\pm 2\%$ levels.

It is clear that the single scatter correction should be applied for all situations in order to achieve acceptable levels of accuracy. However the sphericity correction is only really needed for wide angle views and in general for high solar zenith angles. However, determining the range of viewing geometries for which this correction is required is not a straightforward matter, and further investigation is needed to establish limits of applicability which are consistent with the overall level of accuracy chosen for an operational ozone profile retrieval algorithm with global reach.

By allowing for an acceptable loss of accuracy, a large gain in speed may be obtained using 4/6 stream models. This has great consequence for the performance of operational near-real-time retrievals of ozone profiles, particularly for a high data-rate instrument such as OMI. The choice of an accuracy criterion for the RT model depends on the strategy adopted for the retrieval algorithm, and most importantly on the instrument measurement uncertainty. The aim is to achieve an accuracy level that is better than (or at least equal to) that of the measurements. A measurement accuracy of about 1.5% is in theory obtainable from the GOME, SCIAMACHY and GOME-2 instruments, the main limiting factor being the accuracy of the pre-launch radiometric calculation. Taking this number as a yardstick, the 4 stream model presented here can be expected to simulate radiances to about the same level of accuracy, with the 6 stream model providing a factor of three improvement on the overall accuracy of both radiances and weighting functions. It should be noted that the radiometric calibration error for GOME is actually much greater than 1.5%; additional sources of measurement error for GOME include the instrument degradation now apparent 7 years after launch, and the uncertainty inherent in the polarization correction (up to 10%). In the latter respect, GOME-2 is much better served than GOME; the latter has only 3 polarization measurement devices (PMDs), whereas GOME-2 has some 15 PMDs measuring in two directions of polarization.

We have attempted to quantify only the *forward model error* likely to be encountered in the ozone profile retrieval context; we have not considered other sources of error in the optical properties assumed in the calculation (for example uncertainties in the trace gas cross sections). The 4 and 6 stream models have been installed in an prototype operational algorithm at KNMI designed to retrieve ozone profile information from nadir UV/VIS backscatter measurements from the GOME and GOME-2 instruments. In the follow-up paper to the present work, we carry out a feasibility

study for the operational ozone profile retrieval for the GOME-2 instrument, based on the 4/6 stream models described in the present work. This study will examine the effect of all error sources (including those from the forward model) on the accuracy of the ozone profile retrieval.

Acknowledgements

R.V.O. was supported by The Netherlands Remote Sensing Board (BCRS) under the project *DORAS* 4.1/AP-05. R.J.D.S. was funded from an ozone SAF Visiting Scientist Grant (P-4799-2-00) at KNMI (Royal Dutch Meteorological Institute). The authors would like to thank Piet Stammes for many stimulating discussions on this work.

References

[1] Burrows JP, Weber M, Buchwitz M, Rozanov VV, Ladstaetter-Weisenmeyer A, Richter A, de Beek R, Hoogen R, Bramstadt K, Eichmann KU, Eisinger M, Perner D. The global ozone monitoring experiment (GOME): mission concept and first scientific results. J Atmos Sci 1999;56:151–75.

[2] Callies J, Corpaccioli E, Eisinger M, Lefebvre A, Hahne A. Ozone monitoring by GOME-2 on the METOP satellites. In: Atmospheric ozone, proceedings of the quadrennial ozone symposium, Sapporo, Japan, 2000.

[3] Burrows JP, Chance K, Crutzen P, van Dop H. Geary J, Johnson T, Harris G, Isaksen I, Moortgat G, Muller C, Perner D, Platt U, Pommereau J-P, Rodhe H, Roeckner E, Schneider W, Simon P, Sundquist H, Vercheval J. SCIAMACHY: a European proposal for atmospheric remote sensing from the ESA polar platform. Max-Planck Institut für Chemie, Mainz, Germany, 1988.

[4] Stammes P, Levelt P, de Vries J, Visser H, Kruizinga B, Smorenburg C, Leppelmeier G, Hilsenrath E. Scientific requirements and optical design of the ozone monitoring instrument on EOS-CHEM. In: SPIE Conference on Earth Observing Systems IV, SPIE, vol. 3750. USA: Denver, 1999. p. 221–32.

[5] Bhartia PK, McPeters RD, Mateer CL, Flynn LE, Wellemeyer C. Algorithm for the estimation of vertical ozone profiles from the backscattered ultraviolet technique. J Geophys Res 1996;101:18 793–806.

[6] Munro R, Siddans R, Reburn WJ, Kerridge BJ. Direct measurement of tropospheric ozone distributions from space. Nature 1998;392:168–71.

[7] van der RJA, van Oss RF, Kelder H. Ozone profile retrieval from GOME data. In: Russel JE. editor. Remote sensing of clouds and the atmosphere III, proceedings of SPIE, vol. 3495, Barcelona, Spain: SPIE, 1998. p. 221–9.

[8] Hoogen R, Rozanov V, Burrows J. Ozone profiles from GOME satellite data: algorithm description and first validation. J Geophys Res 1999;104:8263–80.

[9] Chance K, Burrows JP, Perner D, Schneider W. Satellite measurements of atmospheric ozone profiles, including tropospheric ozone, from UV/visible measurements in the nadir geometry: a potential method to retrieve tropospheric ozone. JQSRT 1997;57:467–76.

[10] Spurr RJD, Kurosu TP, Chance KV. A linearized discrete ordinate radiative transfer model for atmospheric remote sensing retrieval. JQSRT 2001;68:689–735.

[11] Spurr RJD. Simultaneous derivation of intensities and weighting functions in a general pseudo-spherical radiative transfer. JQSRT 2002;75:129–75, this issue.

[12] Wiscombe WJ. The delta-M method: rapid yet accurate radiative flux calculations for strongly asymmetric phase functions. J Atmos Sci 1977;34:1408–22.

[13] Nakajima T, Tanaka M. Algorithms for radiative intensity calculations in moderately thick atmospheres using a truncation approximation. JQSRT 1988;40:51–69.

[14] Liou KN. Analytic two-stream and four-stream solutions for radiative transfer. J Atmos Sci 1974;31:1473–5.

[15] Dahlback A, Stamnes K. A new spherical model for computing the radiation field available for photolysis and heating at twilight. Planet Space Sci 1991;39:671–83.

[16] Caudill TR, Flittner DE, Herman BM, Torres O, McPeters RD. Evaluation of the pseudo-spherical approximation for backscattered ultraviolet radiances and ozone retrieval. J Geophys Res 1997;102:3881–90.
[17] Rozanov AV, Rozanov VV, Burrows JP. Combined differential-integral approach for the radiation field computation in a spherical shell atmosphere: Nonlimb geometry. J Geophys Res 2000;105:22 937–42.
[18] Anderson E, Bai Z, Bischof C, Demmel J. Dongarra J, Du Croz J, Greenbaum A, Hammarling S, McKenney A, Ostrouchov S, Sorensen D. LAPACK user's guide. Society for industrial and applied mathematics. 2nd ed. Philadelphia, 1995.
[19] Stamnes K, Conklin P. A new multi-layer discrete ordinate approach to radiative transfer in vertically inhomogeneous atmospheres. JQSRT 1984;31:273.
[20] Thomas GE, Stamnes K. Radiative transfer in the atmosphere and ocean, 1st ed. Cambridge: Cambridge University Press, 1999.
[21] Chandrasekhar S. Radiative transfer. New York: Dover Publications Inc., 1960.
[22] Bass AM, Paur RJ. The UV cross-sections of ozone: 1. Measurements in atmospheric ozone. In: Proceedings of the Quadrennial Ozone Symposium. Greece: Halkidiki, 1985, p. 606–16.
[23] Rodgers CD. Characterization and error analysis of profiles retrieved from remote sounding experiments. J Geophys Res 1990;95:5587.
[24] Stamnes K, Tsay S-C, Laszlo I. DISORT: a general purpose fortran program for discrete-ordinate-method radiative transfer in scattering and emitting layered media: documentation of methodology. NASA Internal Report.
[25] McClatchey R, Fenn RW, Selby JE, Volz FE, Garing JS. Environ Res Pap 411. In: Optical properties of the atmosphere. 3rd edn. Bedford, MA: Air Force Cambridge Res. Lab., 1972.
[26] Chance K, Spurr RJD. Ring effect studies: Rayleigh scattering, including molecular parameters for rotational Raman scattering, and the Fraunhofer spectrum. Appl Opt 1997;36:5224–30.
[27] Bates DR. Rayleigh scattering by air. Planet Space Sci 1984;32:785–90.
[28] Shettle EP, Fenn RW. Models of the aerosols of the lower atmosphere and the effects of humidity variations on their optical properties. Technical Report, AFGL-TR-79-0214, Geophysics Laboratory, Hanscomb AFB, MA 01732, 1979.
[29] Kuze AK, Chance KV. Analysis of cloud top height and cloud coverage from satellites using the O_2 *A* and *B* bands. J Geophys Res 1994;99:14 481–91.
[30] Koelemeijer RBA, Stammes P. A fast method for retrieval of cloud parameters using oxygen A-band measurements from the Global Ozone Monitoring Experiment. J Geophys Res 2001;106:3475–90.
[31] Kurosu TP, Chance KV, Spurr RJD. CRAG—Cloud retreival algorithm for ESA's global ozone monitoring Experiment. In: Proceedings of the European Symposium on Atmospheric Measurements from Space (ESAMS), WPP-161. The Netherlands: Noordwijk, 1999. p. 513–21.
[32] Hsu NC, Herman JR, Bhartia PK, Seftor CJ, Torres O, Gleason JF, Eck TF, Holben BN. Detection of biomass burning smoke from TOMS measurements. Geophys Res Lett 1996;23:745–8.
[33] Herman JR, Bhartia PK, Torres O, Hsu NC, Seftor CJ, Celarier E. Global distribution of absorbing aerosols from Nimbus 7/TOMS data. J Geophys Res 1997;102:16 911–21.
[34] Gleason JF, Hsu NC, Torres O. Biomass burning smoke measured using backscattered ultraviolet radiation: SCAR-B and Brazilian smoke interannual variability. J Geophys Res 1998;103:31 969–78.
[35] van Oss RF. Aerosol retrieval with GOME. In: Proceedings of the European Symposium on Atmospheric Measurements from Space (ESAMS). WPP-161. The Netherlands: Noordwijk, 1999. p. 581–3.